

University of Sheffield

Organic Solar Cells: Solvent the Issues



Daniel Alec Farbowitz

Supervisor: Dr. Jenny Clark

A report submitted in partial fulfilment of the requirements
for the MSc degree in Solar Cell Technology

in the

Department of Physics

September 6, 2021

Declaration

All sentences or passages quoted in this document from other people's work have been specifically acknowledged by clear cross-referencing to author, work and page(s). Any illustrations that are not the work of the author of this report have been used with the explicit permission of the originator and are specifically acknowledged. I understand that failure to do this amounts to plagiarism and will be considered grounds for failure.

Name: Daniel Alec Farbowitz

Signature:

Date: September 6th, 2021

Acknowledgements

I would like to provide thanks to the following people and institutions:

-The University of Sheffield, in particular the administrative members of the Physics department and student disability services

-**Dr. Alastair Buckley** and **Dr. David Lidzey**, my tutors in the Solar Cell Technology program, for all the hours of instruction and enduring my barrage of questions

-**Dr. Buddhapriya Chakrabarti**, my personal tutor, for the frequent check-ins

-My fellow students in the Solar Cell Technology program: **Husssah Alghanem**, **Noor Alotaibi**, **Minchang Chen**, **Rhys Davies**, **Ali Dirjal**, **Tianjing Lu**, **Ziran Wang**, and **Hang Xu**, for countless hours trying to make sense of the material

-**Dr. Jenny Clark**, my dissertation advisor, for engaging me in a whole new world of research

-**Dr. David Bossanyi**, who expertly guided me through the lab and analysis

-**Dr. Matthew Wright** and **Dr. Dimitri Chekulaev**, who opened their labs to me

-**Emma Spooner**, who very patiently walked me through how to make and characterize an organic solar cell

-**Dr. George Sutherland**, for making time to sonicate my samples, no matter how many runs I needed

-**Alexander Auty**, **Sayantan Battychara**, **Daniel Hook**, and **James Pidgeon**, who performed setups of the transient absorption spectroscope and explained the operating principles while doing so

-**Arthur Markus Anton**, **Rahul Jayaprakash**, **Kirsty McGhee**, **Ravi Kumar Venkatraman**, **Shuangqing Wang**, and **all other members of the ultrafast spectroscopy lab group**, who shared their research and listened to my dumb jokes

-**Rachel Kilbride**, who helped explain cell morphology to me

-**Deeba Zahoor**, who gave me coveted access to Dainton Lab

-**Dr. Chang-gyu Hahn**, my psychiatrist/therapist, for keeping me engaged

-**Jonathan Farbowitz**, my brother, for his constant support through crossword solving

-**Diann and Steven Farbowitz**, my parents, for their support in the form of Zoom calls

-**Other members of my family**, for encouraging me to take the next step

-**Lia Cowley**, my best friend, for their constant encouragement when I need it most and **Piper Yuenger**, for making watching bad movies a fun diversion

-**Liz Quinlan**, my partner, for her limitless reserve of compassion and relentless desire to help me, no matter how much Physics was involved.

Abstract

Organic solar cells offer a cleaner, inexpensive alternative to crystalline silicon (c-Si) solar cells. Organic cells are based upon electron transfer from a donor to an acceptor organic material. How the donor and acceptor materials are arranged in the solar cell is of critical importance. The current standard is to process them in solution and spin-coat them as the active layer of the cell. This technique enhances the cell's charge transfer properties. Commonly used solvents, such as chloroform and chlorobenzene, pose a serious health risk. The toxicity of such solvents impede up-scaling production of organic solar cells. One alternative is to remove the solvents by fabricating organic donor:acceptor nanoparticles that are soluble in water (called a nanoparticle ink). The research pursued here demonstrates via transient absorption (TA) spectroscopy that these nanoparticle inks generate charges in their deionized water solution, but charge generation was severely limited after spin-coating, evaporating, and annealing. This result is further complicated by a degree of open air exposure to the films which were used. Taken in conjunction with the existing literature on nanoparticle cells, the result poses more potential factors which hinder the efficiencies of such nanoparticle solar cells. Further results are necessary to better isolate the issue of charge generation between spin-coating and annealing. While morphology is a common explanation for a nanoparticle solar cell's efficiency (or inefficiency) - these results suggest a deeper, chemical or photochemical issue. To improve nanoparticle cell performance, then, photophysical testing (i.e. TA spectroscopy) of the cells with different levels of annealing and open air exposure should be performed. Photophysical methods of observation, like TA spectroscopy, can help isolate where solar cell issues occur and develop a better theoretical understanding of organic solar cells. Cleaner, industrial-scale solar cell fabrication can be achieved when the charge transfer mechanisms of organic materials are better understood.

Contents

Acknowledgements	ii
1 Introduction	1
1.1 Organic Solar Cells	1
1.1.1 Donors and Acceptors	2
1.1.2 Materials and Fabrication	3
1.1.3 Bulk Heterojunction Cells	4
1.1.4 The Solvents Issue	5
1.1.5 Nanoparticle Cells	7
2 Background	9
2.1 Solar Cell Characterization	9
2.1.1 Existing Organic Solar Cells	10
2.1.2 Charge Generation in Organic Solar Cells	10
2.2 NP Ink Cells	11
2.2.1 Nanoparticle Composition	11
2.2.2 Cell Morphology	14
2.2.3 Surfactant	15
2.2.4 Other Considerations	15
2.3 Transient Absorption Spectroscopy	15
2.3.1 Setup	16
2.3.2 Output	16
2.3.3 Relevant TA examples: Guo et al, (2009) and (2010)	18
2.3.4 Existing Nanoparticle TA	20
2.4 Developed Goal	21
3 Methodology	22
3.1 Summary	22
3.2 Material Preparations	24
3.2.1 Solutions	24
3.2.2 Films	25
3.3 NP Ink Adjustments	25
3.4 Spectroscopy	26
3.4.1 Ground (Steady) State Absorption	26
3.4.2 TA Operation	27

3.4.3	Analysis	27
4	Results	28
4.1	OPV Results	28
4.2	Spectroscopy	30
4.2.1	Steady-state Spectra	30
4.2.2	TA Spectra	30
4.2.3	TA Kinetics	32
5	Discussion	35
6	Conclusions	37
	Appendices	46
A	Artefact	47
B	PBDB-T:ITIC Cell Data	48
B.1	Steady-State Spectroscopy	48
B.2	TA Spectroscopy	50
B.2.1	Long-Time TA	50

List of Figures

1.1	An illustration of the energy levels present in an OPV cell with a P3HT/PCBM active layer. Other materials present – Poly(3,4-ethylenedioxythiophene) polystyrene sulfonate (PEDOT:PSS) and Bathocuproine (BCP) – direct the holes (labelled h^+ here) and electrons (e^-), respectively, towards the appropriate metal contact. Reproduced from [1] with the permission of the author.	3
1.2	Chemical diagrams of P3HT (a) and PC ₇₀ BM (b). Reproduced from (a)[2] with permission of the author and (b)[3] (Open Access).	4
1.3	Rough diagrams illustrating the general structure of (a) a bilayer cell with (b) a BHJ cell. The improvement in contact area between donor and acceptor material, while retaining direct paths to the metal contacts generally will result in a more efficient solar cell. Reproduced from [1] with permission from the author.	5
1.4	Diffusion scheme showing light absorption in (a) crystalline P3HT regions or (b) intermixed P3HT:PCBM regions. The transferred electron will diffuse through the (c) isolated PCBM region. The bottom diagram shows that a fast charge state can be formed from the intermixed regions with a 400nm excitation. A 600nm excitation will mainly limit the P3HT excitons to diffusing to the interface. Possible scale sizes included for reference. Reproduced from [4] with permission from the author.	6
1.5	An overview of miniemulsion process – the separate aqueous phase and organic phase on left are mixed and then sonicated (step A) to produce the miniemulsion. Immediately after, (step B) the solvent is evaporated leaving nanoparticles of P3HT and PCBM in the specific example. The ink then goes through dialysis (step C) to remove excess surfactant and achieve the desired molarity. Reproduced from Ref. [5] with permission from the Royal Society of Chemistry.	7
2.1	A diagram of possible organic solar cell processes from light absorption to current generation. Curved shapes at bottom represent undesirable loss pathways.	11

2.2	Possible charge generation pathways shown in terms of an energy-level diagram. The P3HT exciton (P^*) must diffuse (k_{ED}) to encounter the PCBM acceptor (C_{60}). At that point, the charge must transfer (k_{CT}). Since this bound radical pair (BRP) is still electrically bound, it must dissociate (k_{CD}) into free charges, where it can then be carried (k_{CC}) to the electrode. During the process it may decay (k_F) or undergo geminate recombination (k_{GCR}). Reproduced from [4] with permission of the author.	12
2.3	Two depictions of nanoparticle inks on substrate.	12
2.4	A depiction of (a) core-shell nanoparticles and (b) how differently composed nanoparticles may anneal.	13
2.5	(a) Steady-state and (b) TA spectra involving forms of neat P3HT.	16
2.6	Simplified diagram of a TA spectroscope. Reproduced from [6].	17
2.7	A simplified visual of TA operation. Inset left: Energy level diagram of possible transitions. Inset right: A corresponding spectral graph of ΔA vs wavelength. The change in time is shown by color in the lines, and additionally illustrated using arrows. Reproduced from [7].	18
2.8	(left) TA Spectral graph for P3HT:PCBM BHJ films excited by (a) 400nm pump laser and (b) 600nm pump laser. (right) TA kinetics graph showing singlet exciton signal (S) taken at 1200nm, and polaron signal (P) taken at 1000nm after removing overlapping exciton signal. Pump laser (excitation) wavelength is (a) 400nm or (b) 600nm. Both reproduced from [4] with permission from the author.	19
3.1	Diagram illustrating the different pathways followed in the experiments. Followed to completion, this produced two sets of working solar cells (BHJ and NP films) and three sets of optical film samples for TA analysis (neat P3HT, BHJ, and NP).	23
3.2	Images of the NP film cells created in (a) Run 1 and (b) using old inks prior to Run 4.	26
4.1	Sample JV sweeps of both types of P3HT:PCBM solar cell – (a) BHJ and (b) NP. Although tested from 0-1.2V, the graphs scales are adjusted to better observe V_{OC} and J_{SC}	28
4.2	Boxplots demonstrating the PCE values achieved in each run of the (a) BHJ and (b) NP ink cells. Each blue dot represents a PCE for a given run. Note: The ‘forward’ and ‘reverse’ components of the sweep were counted as individual runs.	29
4.3	Steady-state spectra of different forms of (a) neat P3HT and (b) P3HT:PCBM blends in the UV-Visible (UV-Vis) region of the spectrum. Spectra shown in dotted lines are drawn from literature sources.[4]	30
4.4	TA Spectra for (a) neat P3HT and (b) BHJ film. The pump energies for both were estimated as $90\mu J/cm^2$ per pulse.	31
4.5	TA spectra for (a) nanoparticles in solution and (b) NP solution again, but focused in on the NIR region with comparison. Pump pulse energy is $130\mu J/cm^2$ in NIR region, $60\mu J/cm^2$ in UV-Vis region. For Claftron et al. pump pulse energy is $6.5\mu J/cm^2$ [8]	32

4.6	Two graphs depicting TA spectroscopy data from the NP film. (a) A spectral graph, and (b) a kinetics graph.	33
4.7	Kinetics scatterplots of features for all UV-Vis TA at (a) 675nm and (b)750nm. The free polaron feature normally peaks around 700nm in P3HT:PCBM cells. Because the data were taken at different times, pump pulse energies are not quite the same, but all are on the order of $60\mu\text{J}/\text{cm}^2$. Scale is log-log.	34
A.1	Snapshot of the NIR light spectrum generated by the probe laser. The wavelength of the peak value is shown.	47
B.1	Normalized spectra from films produced for each solvent (listed in the graph title). The films that contained neat PBDB-T and neat ITIC were normalized to 0.5 then added to produce the hypothetical 1:1 blend.	49
B.2	Normalized spectra from films produced from different material combinations (listed in title). The baseline films graph has no particular meaning.	49
B.3	Transient absorption graphs of films using chlorobenzene solvent – (a) neat PBDB-T and (b) neat ITIC. Note the peak feature of the PBDB-T exciton at 1.08eV, and the peak feature of the ITIC exciton at 1.28eV.	50
B.4	Transient absorption graphs for blend films using different solvents (listed in the graph titles).	51
B.5	Long-time TA spectra for chlorobenzene films taken at a pump power of (a) $100\mu\text{W}$ and (b) $500\mu\text{W}$	51
B.6	Kinetic graphs for different solvent blends (listed in graph titles) at 2.45eV. The values in the legend (and colors) refer to the pump power in μW for the dataset.	52
B.7	Kinetics graphs comparing the 2.45eV feature for all different solvents at the same pump power – (a) $100\mu\text{W}$ and (b) $10\mu\text{W}$	52

List of Tables

2.1	Several quantities which characterize an OPV cell. These quantities can be directly measured or derived in a circuit with the solar cell. Possible influences of cell morphology on the quantities are included. Summarized from information in [9].	9
2.2	A table of record organic solar cell efficiencies for particular types of OPV with original sources included. All records are based on a single D:A active layer design.	10
2.3	A summary of several papers performing TA spectroscopy on P3HT:PCBM. Feature peaks and their assigned phenomena are listed.	20
4.1	Average values (and standard deviations) of useful solar cell quantities in BHJ film solar cells. Three groups were formed based on different annealing conditions.	29
4.2	Average values (and standard deviations) of useful solar cell quantities in NP film solar cells. Three individual cells were used, but nominally represent the same formation conditions.	29

Chapter 1

Introduction

As the effects of anthropogenic climate change accelerate, humanity faces an unavoidable existential crisis. Economies and ways of living must be radically rethought to prevent further dispersal of greenhouses gasses into the atmosphere. The sector currently dominant in greenhouse gas emissions is energy generation.[10][11][12] Therefore, replacing coal, oil, and gas plants with renewable forms of energy generation will be paramount in addressing the problem directly.

Of the forms of renewable energy, solar power is expected to have the highest growth.[13] Due to this latent potential, addressing the solar industry's sustainability issues has immediate and essential value. The current solar industry is dominated by crystalline silicon (c-Si) cells.[14][15] Lifetime analyses suggest a high CO₂-equivalent cost¹, deriving primarily from the production phase.[16][17] Internationally, there are limited plans in place for recycling, with a notable exception being the EU's WEEE Directive.[16][15] If the solar industry is to become a major part of the energy market, plans to address massive amounts of electronics waste must be implemented in the coming years.[16][15][18]

Significant oversight is required for other byproducts in c-Si cell production. Nitrogen trifluoride, an agent used in cleaning, is an extremely potent greenhouse gas with 16,800 times the global warming potential of carbon dioxide.[19] Furthermore, local conflict has arisen out of a solar firm dumping toxic byproducts in a nearby river.[20] To make progress toward sustainability, the solar industry will have to adapt to newer materials and production.

1.1 Organic Solar Cells

Several methods serve to generate electricity from sunlight. Organic² materials offer a scalable, low-emissions method to fabricate light, flexible solar cells. The benefits of organic solar cells derive from (1) their abundance, (2) their ability to be processed via solution, and (3) limited energy requirements in their fabrication.[21][22][23]

The main hurdle to large-scale implementation of organic solar cells – also referred to as **organic photovoltaics** or **OPVs** – are (1) cell degradation, (2) lower cell efficiencies, and (3) the use of toxic solvents, e.g. chloroform. When the organic material is deposited on a solar cell using a solvent like chloroform, the chloroform will begin to evaporate rapidly,

¹Though far better than non-renewable sources.

²Organic using the chemistry definition – hydrocarbon-containing compounds.

exposing those in the vicinity. To understand why such solvents are used, the inner workings of an organic solar cell must be appreciated.

1.1.1 Donors and Acceptors

The fundamental job of a solar cell is to convert incoming light into separated charges. The region in which both light absorption and charge separation occur is referred to as the **active layer** of the cell. Eventually, opposing charges are further separated until they reach metal contacts and form the current in a circuit.

Inorganic solar cells are typically crystalline semiconductors that direct free charges via built-in electrical potentials. When the inorganic semiconductor absorbs light, the material goes into an excited state, where an electron is promoted to the conduction band, where it is free to move. This leaves behind a net positive charge in the valence band tied to the molecule. Since the valence band is readily filled via other nearby electrons, the positive charge can be thought of as its own mobile charge carrier, referred to as a **hole**.

In summary, light absorption in materials creates an electron-hole pair, referred to as an **exciton**. In inorganic semiconductors, these excitons have a very small binding energy³ (1-10 meV) which is easily overcome by thermal energy in the cell. In organic semiconductors, the binding energy for excitons is at least an order of magnitude larger (100-1000 meV). This energy requirement in converting excitons to charges (a.k.a. **polarons**) also explains some of the inherent inefficiency in an organic solar cell. Large potential gaps are needed in order to separate the electron and hole.

The standard for achieving charge separation in organic cells are **donor-** and **acceptor-**type molecules. The donor and acceptor molecules are defined by the relative energies of their excited states. A donor's first excited state will be higher energy than the acceptor's charged state. In the absence of external influence, materials will adopt lower energy states when available. Therefore, when in close proximity to one another, a donor will readily donate an electron to the acceptor.

A donor exciton's electron is attracted to the donor molecule by electric (Coloumbic) force. The electron is only freed when the excited donor molecule comes into contact with an acceptor molecule. Due to the energy difference between the excited states in the donor and acceptor materials, the once-bound electron is able preferentially transfer over to an acceptor molecule.⁴

While the donor and acceptor materials separate charges in the active layer, the charges must be further extracted to their respective electrodes in a solar cell to produce current in an attached circuit. Thus, in practice, the active layer is sandwiched between an **electron-transport** and a **hole-transport layer** (BCP and PEDOT:PSS, respectively, in Figure 1.1). These layers have progressively lower potentials for electrons and higher potentials for holes, which direct them towards their respective electrodes.

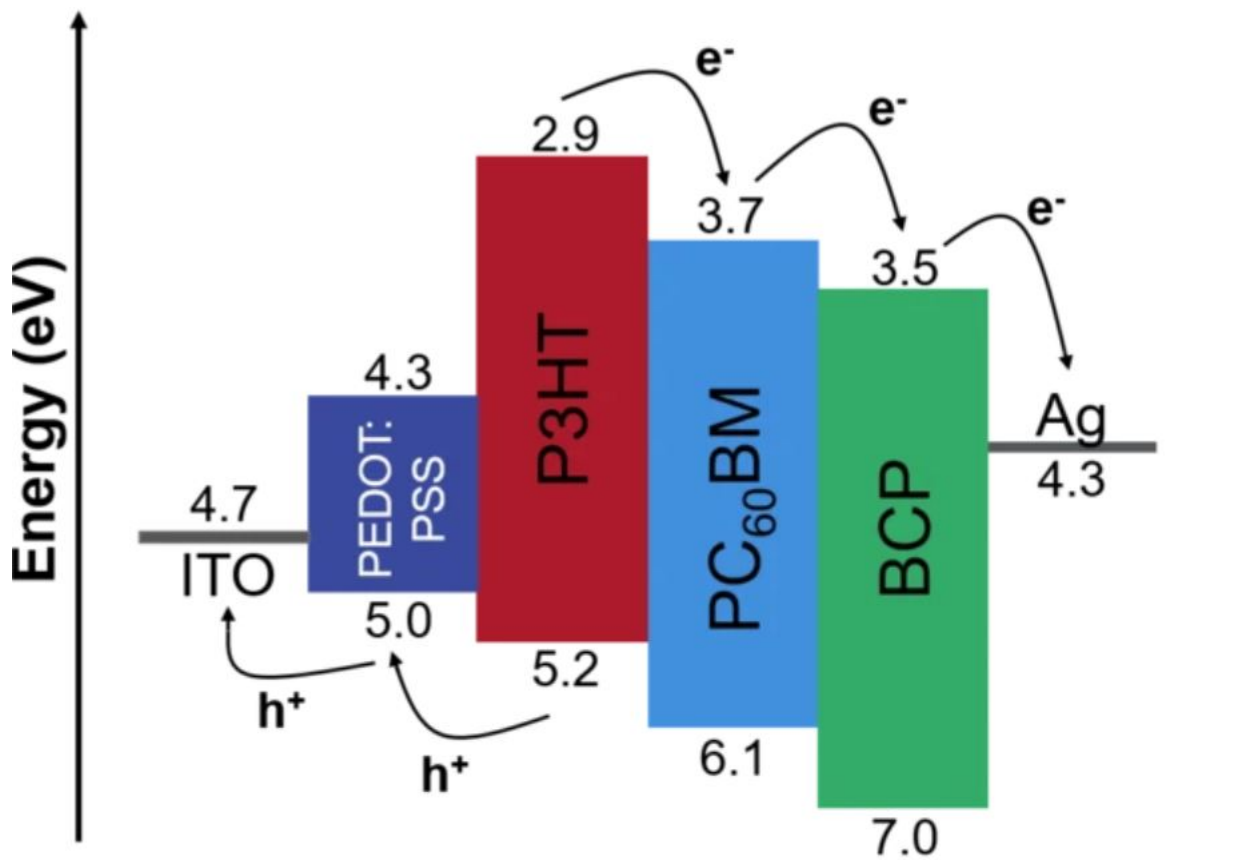


Figure 1.1: An illustration of the energy levels present in an OPV cell with a P3HT/PCBM active layer. Other materials present – Poly(3,4-ethylenedioxythiophene) polystyrene sulfonate (PEDOT:PSS) and Bathocuproine (BCP) – direct the holes (labelled h^+ here) and electrons (e^-), respectively, towards the appropriate metal contact. Reproduced from [1] with the permission of the author.

1.1.2 Materials and Fabrication

A commonly studied donor:acceptor pair is the polymer Poly(3-hexylthiophene-2,5-diyl) (also known as **P3HT**) and the fullerene [6,6]-Phenyl C₇₀ butyric acid methyl ester (**PCBM**⁵). P3HT serves as the donor; PCBM is the acceptor. They are relatively inexpensive materials from which to produce organic solar cells.[24] The combination has been studied extensively.[25][24][9][26] Thus, they are a donor:acceptor (**D:A**) pair well-suited to the focus of this dissertation. They will be used as specific examples of D:A materials.

To process organic solar cells, the (commonly) solid organic materials must be put into a liquid phase. This involves dissolution into a solvent. When organic materials contain long

³Deriving from their mutual electrical attraction.

⁴The now positively-charged donor and negatively-charged acceptor may still be electrically bound to each other. This is known as a **paired polaron**.

⁵Several variations on the fullerene exist - e.g. C₆₀, C₆₁, C₇₀, C₇₁. These are all subsumed under the label PCBM and distinguished where necessary.

P3HT

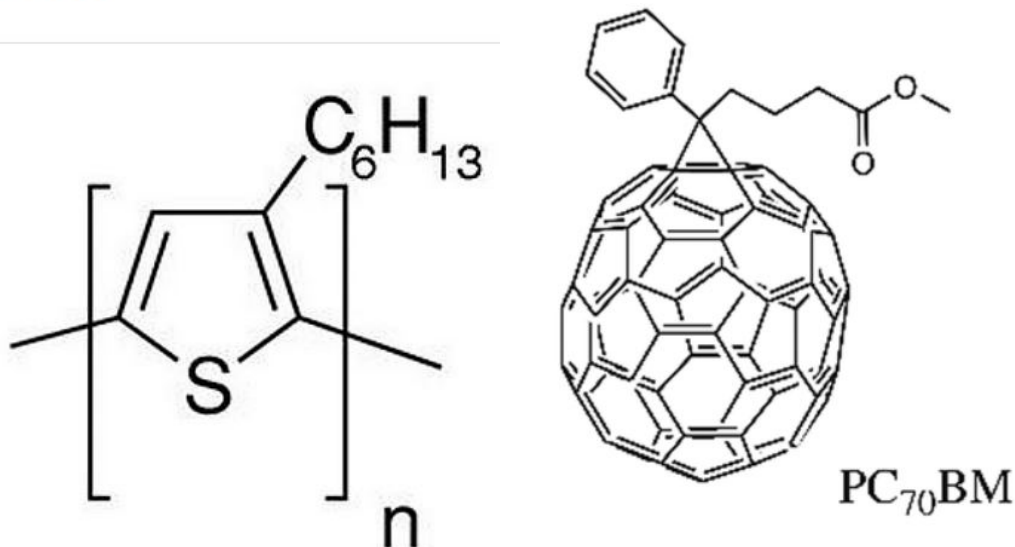


Figure 1.2: Chemical diagrams of P3HT (a) and PC₇₀BM (b). Reproduced from (a)[2] with permission of the author and (b)[3] (Open Access).

chains of hydrocarbons, they are not soluble in water and other common solvents. Solvents which readily mix such organic materials are chloroform and chlorobenzene.⁶ Solvents offer the ability to rapidly produce organic solar cells via roll-to-roll printing.[22] For research purposes, however, the resulting solution is mainly deposited on a substrate via spin-coating.[21]

Once mixed into solution, the liquid mixture (or **organic phase**) is able to be spin-coated onto a substrate. This involves securing the substrate onto a platform, depositing a volume of organic phase on the substrate, and allowing the platform to spin at high rotational speeds (thousands of rotations per minute) for brief time intervals (0-120s).⁷ This high-speed process removes excess solution, coating a nearly-uniform thickness liquid layer atop the substrate. The substrate is then heated (or **annealed**) to remove the solvent and allow the organic materials to solidify. The subsequent arrangement of D:A materials due to these processes defines the cell's **morphology**.

1.1.3 Bulk Heterojunction Cells

In order to achieve charge separation more efficiently, OPV research has recently moved away from creating singular donor:acceptor layers, i.e. bilayer cells (Figure 1.3a).[21][3] If the aforementioned spin-coating process is performed, the result instead is a intermixed layer of donor:acceptor molecules in solution. Heating such an active layer does several things: (1) The donor and acceptor materials begin to segregate; (2) the solvent evaporates; and (3) the

⁶While some research has focused on using less hazardous solvents, the ability of chloroform and chlorobenzene to readily dissolve organic materials has made them the standard.

⁷This method is referred to as static spin-coating. Dynamic spin-coating deposits the solution while the substrate is rotating.

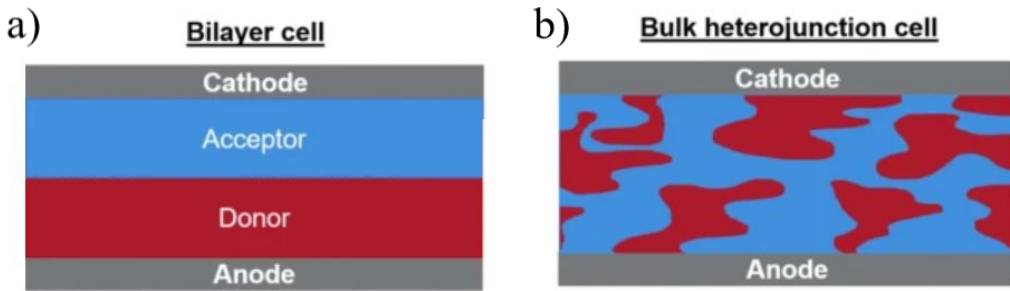


Figure 1.3: Rough diagrams illustrating the general structure of (a) a bilayer cell with (b) a BHJ cell. The improvement in contact area between donor and acceptor material, while retaining direct paths to the metal contacts generally will result in a more efficient solar cell. Reproduced from [1] with permission from the author.

layer solidifies.⁸

By mixing the D:A molecules in a solvent, spin-coating, and thermally annealing, researchers achieve what is known as a bulk heterojunction (**BHJ**) morphology.[21][27] In a BHJ active layer, there are distinct, amorphous-shaped regions of separate donor and acceptor, with an intermixed region at their interfaces, as seen in Figure 1.3b. Also shown in Figure 1.4, such distinct regions can have separation on the order of nanometers. This small-scale morphology facilitates excited state molecules (excitons) making contact with another material layer before the excitons decay back into the ground state.

If a donor exciton reaches the donor-acceptor interface (k_{ED} in Figure 1.4), an electron is able to transfer to the acceptor material. This will create two interface molecules with opposite charge (called a **paired polaron**). Once the charges separate from one another (**free polarons**), the segregated regions of donor and acceptor facilitate movement of the charges towards their respective electrodes. Put another way, the optimization of such solar cells could be thought of as maximizing the interface area of donor and acceptor, while leaving a clear path of uniform donor or acceptor phase for newly-separated charges to reach their respective electrode.

1.1.4 The Solvents Issue

BHJ cells have been dominant in organic solar cell research.[21][22] However, the need to mix D:A materials in hazardous solvents to achieve a BHJ morphology has focused some research on alternatives.

One idea is to use less hazardous solvents, e.g. ortho-Xylene. Organic D:A materials are generally less soluble in ortho-Xylene, requiring heating to dissolve and sometimes leading to lower cell efficiencies. An experiment in this field was pursued during the course of the dissertation, but is not the focus. It was pursued when lab restrictions due to COVID made completion of the initial project less certain. The results of those experiments can be found in Appendix B.

Other cell designs altogether are possible, driven by the recent creation of nanoparticle

⁸The required temperature (or glass temperature) depends on the material properties.

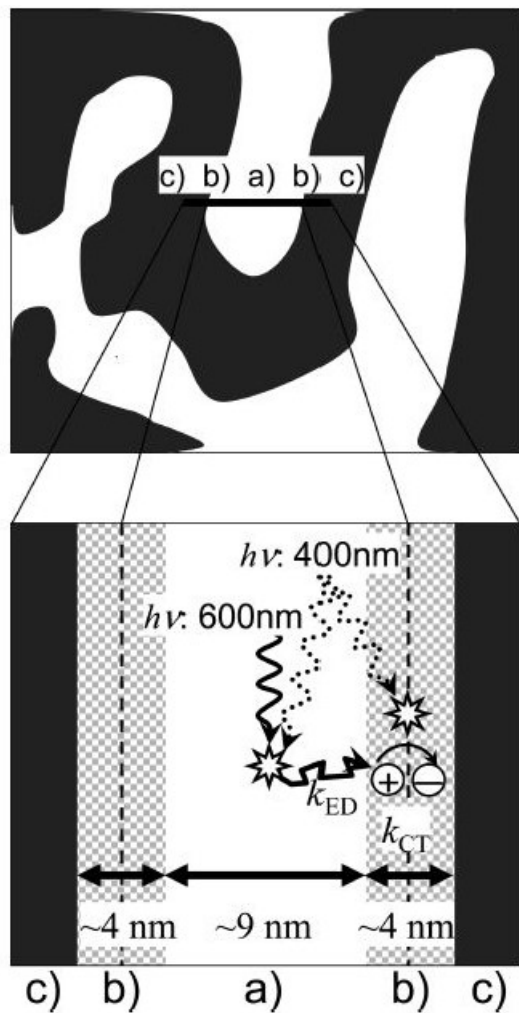


Figure 1.4: Diffusion scheme showing light absorption in (a) crystalline P3HT regions or (b) intermixed P3HT:PCBM regions. The transferred electron will diffuse through the (c) isolated PCBM region. The bottom diagram shows that a fast charge state can be formed from the intermixed regions with a 400nm excitation. A 600nm excitation will mainly limit the P3HT excitons to diffusing to the interface. Possible scale sizes included for reference. Reproduced from [4] with permission from the author.

(NP) solar cells.[28] In addition to the potential to improve upon BHJ morphology, organic NP cells directly address the issue of hazardous solvents.

1.1.5 Nanoparticle Cells

This method for cleaner organic materials involves making the organic materials soluble in water. Water allows for the same rapid, solution-based printing. While the creation of NP cells begins using the same solvents, these solvents can be removed in isolation prior to depositing the active layer. This smaller-scale evaporation keeps hazardous solvents in a closed cycle that is far less costly than vacuuming post-processing.

A common method for nanoparticle fabrication is known as **miniemulsion**.[28]

Miniemulsion process

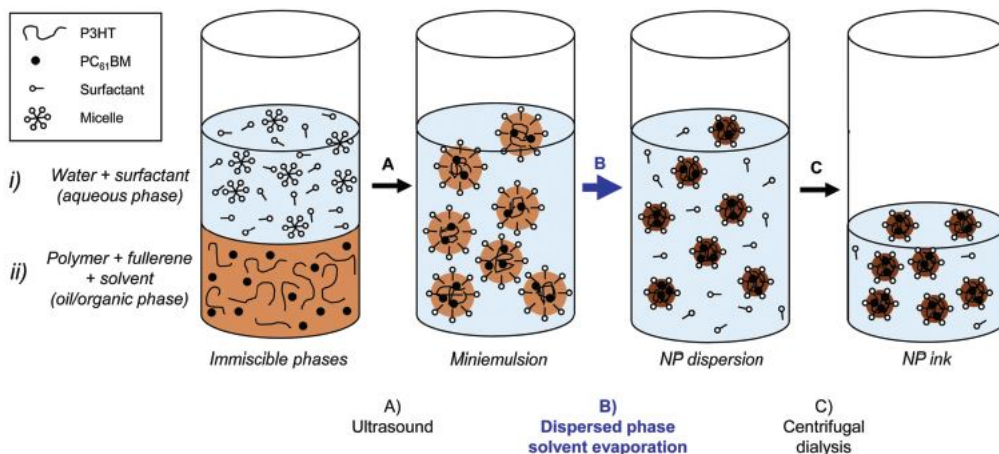


Figure 1.5: An overview of miniemulsion process – the separate aqueous phase and organic phase on left are mixed and then sonicated (step A) to produce the miniemulsion. Immediately after, (step B) the solvent is evaporated leaving nanoparticles of P3HT and PCBM in the specific example. The ink then goes through dialysis (step C) to remove excess surfactant and achieve the desired molarity. Reproduced from Ref. [5] with permission from the Royal Society of Chemistry.

Typical D:A materials cannot be mixed with water directly. Rather, they are mixed in solvent first, forming the organic phase⁹. This organic phase is then mixed with an **aqueous phase** of water and surfactant (i.e. soap) as shown in Figure 1.5. These two phases are continuously mixed so that, like soapy water and oil, the hydrophobic tail of the surfactant joins with the organic phase, leaving large drops of organic phase bounded by hydrophilic surfactant heads. Then this **macroemulsion** is subject to high-amplitude, high-frequency sound waves (i.e. sonication) so that shear forces begin to break apart the droplets into smaller spheres. Immediately after, the solvent is evaporated, leaving behind the D:A materials embedded in surfactant. Dialysis is performed on this dispersion to remove excess

⁹This is the same basic solution generated for a traditional bulk heterojunction cell.

surfactant present in the water and achieve the desired solids content. The resulting solution is referred to as a **nanoparticle ink**. In a literature survey, the miniemulsion method was the most common method of producing organic NP solar cells. [9]

Through variation on the miniemulsion process, individual nanoparticles can be composed of pure donor, pure acceptor, or a blend. The extra degree of control offered by the miniemulsion process suggests that one can reproduce or improve upon BHJ morphology.

Because they propose greater control over cell design without dangerous solvents post-processing, NP ink cells are at the forefront of cleaner solar energy. Despite the great promise in NP ink cells, efficiencies still lag behind their BHJ counterparts.[9] (also see Table 2.2) The reasons for this efficiency drop are the subject of extensive study.

Chapter 2

Background

Nanoparticle ink solar cells, though apparently offering water-based solution processing and greater morphology control, tend not to convert solar power as efficiently as BHJ solar cells using similar materials.[9] To better understand the efficiency issues in NP ink solar cells, solar cell characterization methods will first be discussed. Subsequently, observational and comparative studies of NP ink cells will be reviewed.

2.1 Solar Cell Characterization

A core solar cell property is its power conversion efficiency (**PCE**). It is the power output of the solar cell upon illumination, divided by the power incident on the cell. Put another way, it is the proportion of light energy reaching the cell that gets converted into useful electrical energy.

Other important quantities to the cell are listed in the following table:

Quantity	Symbol	Description	Influencing factors
Open circuit voltage	V_{OC}	Voltage when circuit between electrodes is open (or infinite resistance)	-Energy gap between D:A states -Recombination -Pinholes in device layers -Area of D:A Interface
Short circuit current	J_{SC}	Current when resistanceless circuit ¹ between electrodes is closed	-Light absorption of materials -Geminate recombination -Charge mobility
Fill factor	FF	Ideality factor based on the maximum power output of the cell divided by $J_{SC} \times V_{OC}$	-Charge recombination -Charge transport

Table 2.1: Several quantities which characterize an OPV cell. These quantities can be directly measured or derived in a circuit with the solar cell. Possible influences of cell morphology on the quantities are included. Summarized from information in [9].

They can all be related by the following equations:

$$PCE = \frac{P_{out}}{P_{in}} = \frac{FF \times J_{SC} \times V_{OC}}{P_{in}} \quad (2.1)$$

where P_{in} is the power from light incident on the solar cell and P_{out} is the maximum power output by the cell.

¹Aside from internal resistance in the solar cell.

These quantities can be measured by placing the solar cell into a circuit when light² is incident on the cell. The voltage is varied and the resulting current is measured. All four quantities can be determined from the aforementioned **JV sweep**.

2.1.1 Existing Organic Solar Cells

Organic Solar Cell Record PCEs				
Type of organic solar cell	PCE	D:A Materials	Source	Notes
BHJ	17.6%	D18:Y6	[29]	Replaced by 18.7% [30]
NP	7.50%	PBQ-QF:ITIC	[31]	Unique method, see 2.2.3
NP using miniemulsion	3.80%	PBDTTPD:PC ₇₁ BM	[32]	
BHJ - P3HT:PCBM	6.65%	P3HT:PC ₆₁ BM	[33]	
NP - P3HT:PCBM	2.15%	P3HT:PC ₆₁ BM	[34], [35]	Tied for record

Table 2.2: A table of record organic solar cell efficiencies for particular types of OPV with original sources included. All records are based on a single D:A active layer design.

Organic solar cell research can be thought of as finding the materials, mixture thereof, deposition process, treatment, and lab conditions which maximize PCE. Development focuses on other goals like scalability, longevity, and safe production. Through improvements in both materials and morphology, organic solar cell efficiencies have increased in the past 35 years from 1%[36] to its current record of 18.7%.[30]

2.1.2 Charge Generation in Organic Solar Cells

As mentioned in Section 1.1.3, to extract an optimal amount of photocurrent, two rules are to 1) maximize the amount of surface area between donor and acceptor materials, and 2) have each domain provide a clear path to its respective metal contact. These general guidelines arise as a result of the fundamental charge processes which occur in an OPV.

These processes make up another useful quantity. The Internal Quantum Efficiency (**IQE**) of a solar cell is, in essence, what proportion of the photons (of a given wavelength) from incident light are ultimately converted to free polarons³ at the electrodes. It is closely tied to, though not the same as, PCE. Separating IQE into the efficiencies of its component processes yields an equation⁴ like

$$IQE = \eta_{Abs} \cdot \eta_{ED} \cdot \eta_{CT} \cdot \eta_{CD} \cdot \eta_{CC}. \quad (2.2)$$

The η notation refers to the efficiency in each process, i.e. what proportion of input molecules undergo the process in question. The successive processes given a subscript in Equation 2.2 are (1) light absorption / exciton generation in the organic material, (2) exciton diffusion to the donor/acceptor interface, (3) successful charge transfer once at the interface, (4) charge diffusion (i.e. separation) from the interface, and (5) charges carried successfully to the electrode.[37]

²Generally from a solar simulator.

³To refresh: unbound charge pairs.

⁴Initially from [37], adapted with similar notation to [4].

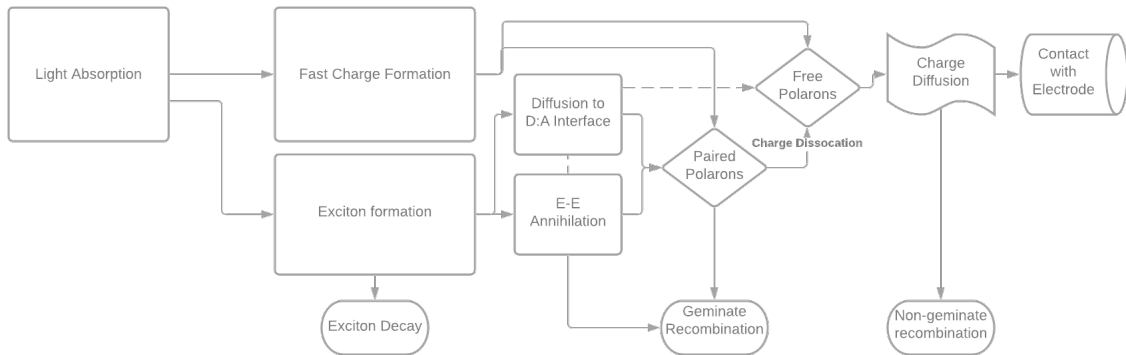


Figure 2.1: A diagram of possible organic solar cell processes from light absorption to current generation. Curved shapes at bottom represent undesirable loss pathways.

The number of figures in Equation 2.2 suggest there are many routes for an exciton or charge to be quenched before reaching the electrode. An exciton has a natural decay time depending on the type of molecule – meaning it may return to the ground state before reaching the interface altogether.⁵ If the interface is reached, the electron will likely transfer over to the acceptor (see figure 2.2). However, the newly created positive and negative charge pair may remain bound to one another by their electrical attraction. Bound and unbound charges may recombine with their initially paired charge (**geminate recombination**) or with other attractive, free charges (**non-geminate recombination**).

As referenced in Table 2.1, OPV circuit measurements can provide some details about the cell’s function. These quantities are interconnected with multiple internal processes. Optical methods can be used to isolate and further infer the inner workings of a cell.[4][37][38] Charge generation processes have been the subject of much investigation to determine why NP ink solar cell efficiencies are lacking.

2.2 NP Ink Cells

Paraphrasing Marks et al (2019)[5], there are three main explanations of the efficiency issue offered in the literature: (1) nanoparticle composition, (2) the resulting cell’s morphology, and (3) the use of surfactant.

2.2.1 Nanoparticle Composition

Shape and Sizes

Nanoparticles made via miniemulsion almost exclusively adopt a spherical shape.[9] They range from 5-150 nm in diameter.[9][39][40] If the NP ink is concentrated enough, one deposition is considered sufficient for a homogeneous active layer.[39][5] When nanoparticles are

⁵Combining this decay time with the exciton mobility gives the **exciton diffusion length**, i.e. how far an exciton will typically travel before decay.

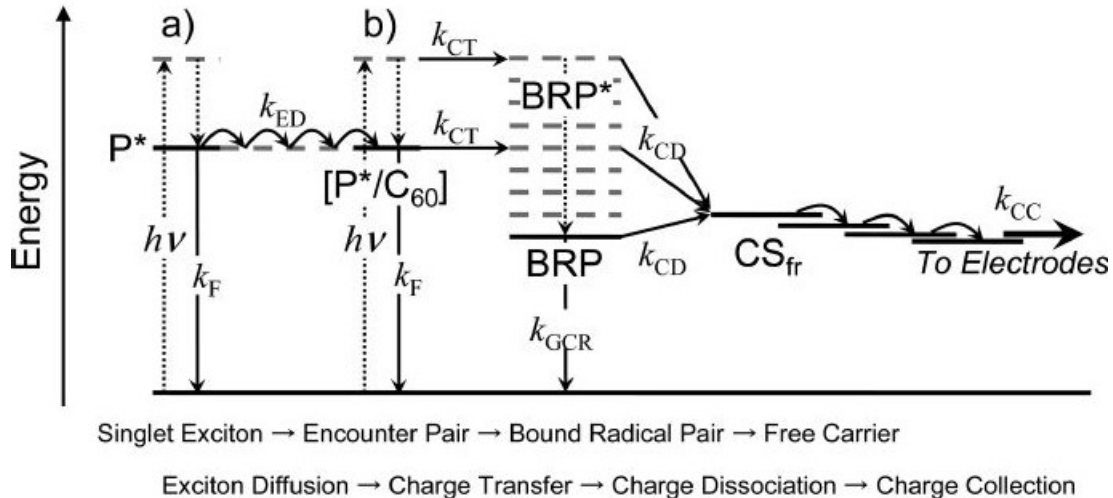
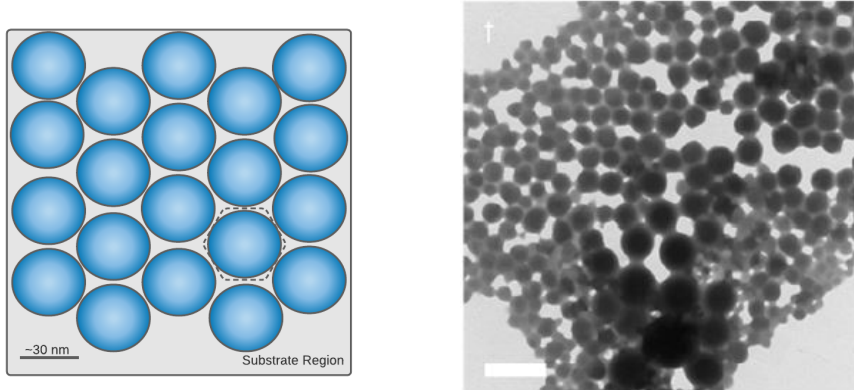


Figure 2.2: Possible charge generation pathways shown in terms of an energy-level diagram. The P3HT exciton (P^*) must diffuse (k_{ED}) to encounter the PCBM acceptor (C_{60}). At that point, the charge must transfer (k_{CT}). Since this bound radical pair (BRP) is still electrically bound, it must dissociate (k_{CD}) into free charges, where it can then be carried (k_{CC}) to the electrode. During the process it may decay (k_F) or undergo geminate recombination (k_{GCR}). Reproduced from [4] with permission of the author.

sufficiently small ($\sim 30\text{nm}$) they adopt a hexagonal close-packed structure[41], as shown in Figure 2.3.



(a) Based on imaging from literature, a model of what a small portion of substrate spin-coated with nanoparticles (blue spheres) may look like based on the nanoparticles' expected size. The dotted line represents a hexagonal unit of packing.

(b) Scanning electron microscope imaging of a nanoparticle film. The white bar represents 600nm. Reproduced from [42] with the permission of the author.

Figure 2.3: Two depictions of nanoparticle inks on substrate.

Nanoparticle size can be controlled at several points in the fabrication process. With re-

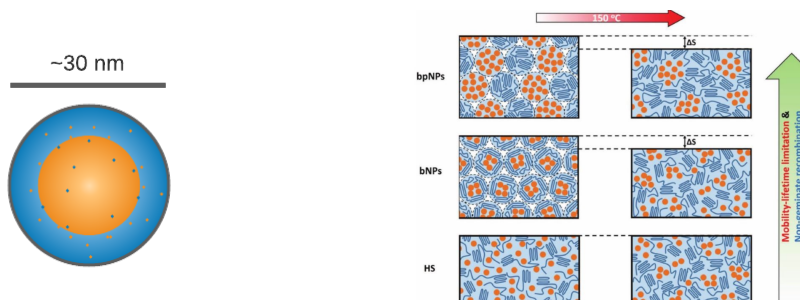
gard to miniemulsion, the size can be controlled by surfactant type, surfactant concentration[43], sonication power, and sonication time.[44] The miniemulsion procedure used in this experiment is based on Marks et al (2019). Using scanning electron microscopy (SEM), their nanoparticles were estimated to have a mean diameter of 29 (± 12) nm.[5]

Internal Nanoparticle Composition

During the miniemulsion process, nanoparticles naturally adopt a core-shell morphology, as shown in Figure 2.4a[45][9][5]. Scanning transmission X-ray microscopy measurements show both the P3HT-rich shell and PCBM-rich core are around 70% of their respective material. The remaining 30% is composed of the other material.[45] These regions can be more intermixed (~60%:40%) when the evaporation step is rapid.⁶[5] In this case the PCEs were improved slightly (1.0% for slow evaporation to 1.2% for rapid evaporation). This increase was not considered enough to identify core-shell distribution as the main issue.[5]

Without alteration to the core-shell structure, charges may become trapped in the acceptor core.[46][47][48][49] Annealing can alter this morphology, leading to improved cell efficiencies.[50][51][9]

It is possible to generate separate P3HT nanoparticles and PCBM nanoparticles. Some experiments created cells using a mixture of P3HT NPs and PCBM NPs that were then annealed.[52][34] Holmes et al (2018) note a ‘third phase’ that develops after annealing which improved exciton diffusion and dissociation in the cell. Separate nanoparticles did not show PCE improvements in studies thus far, but remains an active area of research.[9][39]



(a) A model of what a cross-section of a core-shell nanoparticle may look like. P3HT is represented in blue, PCBM is represented in orange. Although they don't arrange precisely this way, the small dots of blue and orange are meant to represent the actual intermixing of D:A materials in alternate domains.

(b) Diagrams showing – in downward succession – the effects of annealing on separate NPs, core-shell NPs, and BHJ films. Reproduced from [39].

Figure 2.4: A depiction of (a) core-shell nanoparticles and (b) how differently composed nanoparticles may anneal.

⁶Several seconds, compared to several hours. Rapid evaporation gives the donor materials less time to connect with one another through diffusion.

2.2.2 Cell Morphology

Annealing

In principle, after deposition and annealing, NP cells should blend and emulate BHJ structures. The formation of the nanoparticles allow for better control of the morphology rather than the random process of spin-coating. s.[9][42]

After initial deposition, the amount of contact between the nanoparticles and other layers is limited, leading to very low PCEs. The general trend in literature is improvement in PCEs due to annealing.[42][53][54][41] However, it is also possible to ‘overanneal’.[45][55][56]

The primary effect of annealing is to allow the particles to spread out, filling in space and improving polymer connections as seen in Figure 2.4b. Depending on annealing conditions, it can lead to an increase in inter-mixture. The positive effect of intermixed regions are increased charge formation, due to excitons easily finding alternate D:A regions. The negative effect of intermixed regions is the lack of direct pathways to their respective electrodes.

Alternatively, the increase in diffusion with longer anneals and higher temperatures can attract similar D:A materials, leading to more segregated D:A regions.[9] The benefits and drawbacks of segregation are reversed – increased charge mobility at the cost of decreased charge generation, particularly if segregated regions become larger than the exciton diffusion length.

Aside from temperature conditions, other factors affecting annealing include (1) D:A material type, (2) molecular weight – especially of the donor material, and (3) crystallinity in the materials.[56][55][45] Thus, there is no uniform annealing process and conditions must be considered carefully.

Crystallinity and Diffusion

Charge generation is linked to the ability of excitons to diffuse and find alternate D:A material. As a polymer, regio-regular⁷ P3HT can form large crystalline domains. Regions of uniform, crystalline P3HT (**cP3HT**) improve charge transport.[9][52][57]

The amount of crystallinity in P3HT increases with annealing. Slowing the solvent evaporation process⁸ has been shown to further segregate the P3HT-rich and PCBM-rich regions, as well as lead to more crystalline P3HT domains. One can reasonably expect this to be the case for nanoparticles as well, as crystalline donor is observed in the shell region.[48][9][52] Holmes et al (2014) observed efficiency results in both BHJ and NPs cells for different molecular weights of P3HT.[61] Although larger molecular weights (and therefore larger polymer chains) were generally favorable in BHJ cells, this was not the case in NP cells. It was proposed that the large P3HT chains inhibit the motion of the PCBM cores during annealing.[45][61]

Incorrect annealing conditions can lead to broad phase-segregation of P3HT and PCBM.[56] Beyond the overall size, the organization of the domains is fundamental – linked to both polymer structure, nanoparticle organization, and annealing.

⁷Arranged alternating from head to tail.

⁸This can be achieved by choice of temperature[53], solvent[58], or surfactant[59][60].

2.2.3 Surfactant

The use of surfactant in miniemulsion is a double-edged sword. Surfactant helps keep the inks stable in solution for more than 6 months.[44] On the other hand, residual surfactant creates impurities in the cell can lead to further defects and can create additional charge trapping centers.[62]

The most commonly used form of surfactant for miniemulsion is sodium dodecyl sulfate (SDS).[9] In SDS, the negatively charged heads repulse surfactant heads in other particles, preventing the joining of nanoparticles (aggregation).[44] This stability of the inks is particularly important for industrial application.

The current PCE record holder for NP cells was able to strip surfactant off the nanoparticles.[31] In this paper, the nanoprecipitation method was used.⁹ The team focused nanoparticle formation in regions of the surfactant Pluronic F127. Immediately prior to deposition, the surfactant was stripped off, resulting in a peak efficiency of 7.5%.[31]

2.2.4 Other Considerations

In general, water and air tend to be unfavorable and encourage the degradation of OPVs.[21] Therefore, further clarification about the water content and its effects should be crucial.

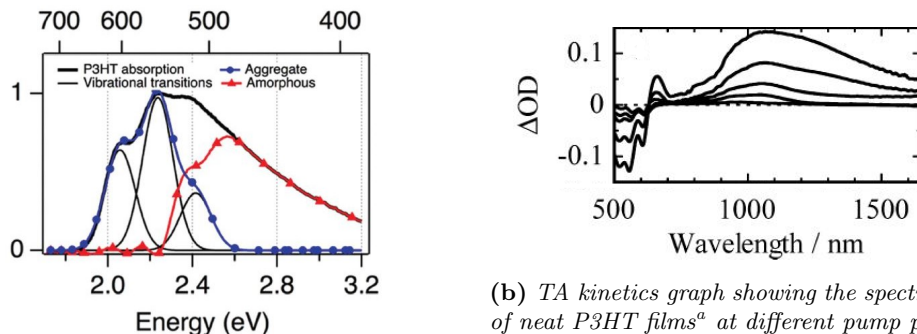
The factors which dictate a NP solar cells performance are many. As illustrated by Table 2.1, the charge generation and charge mobility quantities of a cell have complex relationships to their JV results. Transient absorption (TA) spectroscopy can aid in visualizing properties like exciton diffusion, exciton decay, charge generation, and recombination. The remainder of this section will be spent on its description and TA spectroscopy papers relevant to P3HT:PCBM cells.

2.3 Transient Absorption Spectroscopy

By exposing a sample to a white light spectrum, traditional steady-state (or ground-state) spectroscopy shows the user how the sample molecules absorb from their ground-state energy. Important details about the composition of the sample can be discerned from this process. For example, the proportion of crystallinity in P3HT can be determined from its steady-state spectrum – shown in Figure 2.5a. However, the sample’s behavior in its excited states are inaccessible with this method.

Transient absorption (TA) spectroscopy involves exciting a sample; the excited sample is hit by a probe spectrum almost immediately after. This process allows the user to observe the behavior of the sample in the excited state.[65]

Two lasers are generally used to perform TA. The laser responsible for exciting the sample is referred to as the **pump laser**. The laser sent through a crystal to generate a full spectrum of light (via non-linear optical effects) is referred to as the **probe laser**. Both lasers are pulsed, rather than continuous.



(a) Steady-state spectrum applying the aggregate model to demonstrate portions of the spectrum for crystalline (or aggregate) P3HT and amorphous P3HT for nanoparticles. Reproduced from [48] with permission from the Royal Society of Chemistry.

(b) TA kinetics graph showing the spectrum of neat P3HT films^a at different pump powers. Times were (successively closer to the zero line for Δt) 0, 1, 10, 100, and 3000 ps. Reproduced from [64] with permission from the author.

^aNeat P3HT referring to P3HT on its own.

Figure 2.5: (a) Steady-state and (b) TA spectra involving forms of neat P3HT.

2.3.1 Setup

To vary the amount of time between when the pump pulse hits the sample and when the probe pulse hits the sample, a delay stage is placed in the path of one of the lasers (which laser is irrelevant). The delay stage is made up of four mirrors, two of which move together (see Figure 2.6). Sliding the mirrors back and forth changes the distance required for the light to travel, thereby altering the time at which the laser pulse arrives at the sample. This mechanism allows the user to control the difference in time (Δt) when the pump and probe pulses arrive at the sample.

By altering the time at which the pulses arrive at the sample, the user gets a ‘snapshot’ of what the sample looks like a certain point in time after excitation. Assembling many of these snapshots at various time differences demonstrates the time evolution of a sample’s excited state. In the ultrafast transient absorption spectroscopy performed in the Lord Porter laser lab, the time resolution is on the order of 100s of femtoseconds.

The quantity measured is change in the sample’s absorbance (ΔA). A spectrometer receives the light after it has passed through the sample. In each shot, the sample is struck with the probe pulse alone, then with the pump and probe pulses in succession. The probe pulse alone gives the absorbance of the sample in the ground state, since there was no prior excitation. The combined pump-probe pulses give the absorbance of the sample at Δt , after the sample is excited, shown in Figure 2.7. The difference between the two absorbance spectra, then, demonstrates what changed in the sample due to the prior excitation. This can give the user a sense of the occupancy of new states immediately after excitation.

2.3.2 Output

The product of this process is three-dimensional data – ΔA vs. Time vs. Wavelength. Instead of graphing in three dimensions, two general methods are common for displaying this data

⁹For more info, see [63].

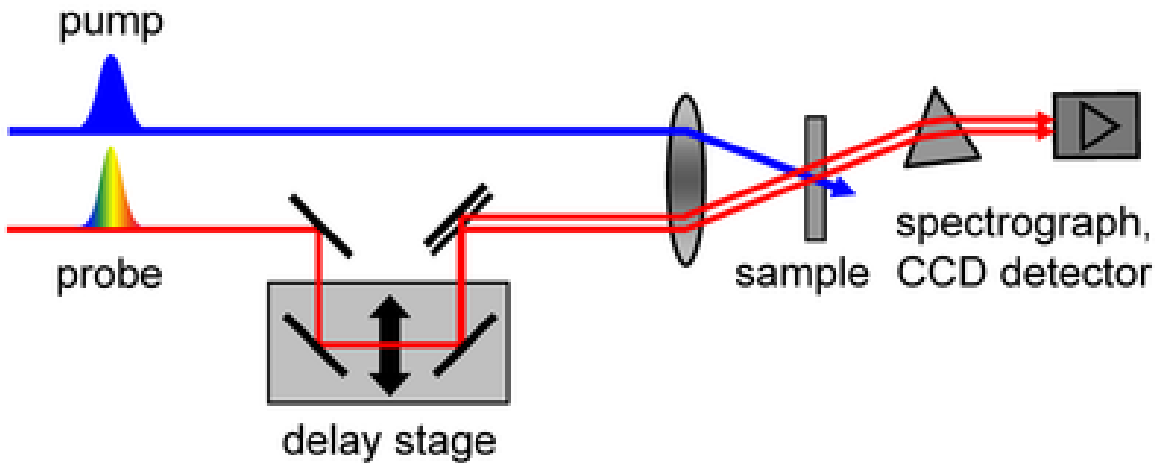


Figure 2.6: Simplified diagram of a TA spectroscope. Reproduced from [6].

- (1) a spectral graph, which plots ΔA against the light spectrum at fixed times, and (2) a kinetics graph, which plots ΔA against time at fixed wavelengths.

Spectral Features

In a spectral graph (as in Figure 2.7, inset right), negative features in ΔA generally occur as a result of fewer molecules in the sample being in the ground state. In other words, the ground state of the molecule would normally absorb the light of a specific wavelength, but will not absorb that wavelength from an excited state. These features are referred to as the **ground state bleach**¹⁰ (GSB).[65]

Positive features in ΔA suggest new states occupying the sample, i.e. new absorbance by an excited state feature. The number of features vary because multiple processes can occur in the excited state. In addition to excitons, with an organic solar cell sample, one should expect charged states (polarons). These polarons can also come in different types - paired and free - which can have unique absorbances. Absorbances tend to be broad in organic molecules. As a result, positive features in a spectral graph can overlap. They may need to be distinguished from one another by observing kinetics at specific wavelengths.

Kinetic Features

Kinetic graphs of ΔA are important for distinguishing features and determining lifetimes. Kinetics are performed by selecting a particular wavelength to observe (or region of wavelength to average). Typically, the wavelength is chosen based on distinct peaks in TA spectra or known features. The signal at that wavelength is plotted against time.

Because of the complex relationship between processes, kinetics will likely involve some combination of exponential and power law decays. One term in the exponential function is a time constant – determining this time constant gives a sense for the time scales on which

¹⁰Negative features may also arise as a result of stimulated emission in the sample. This will cause coherent light to arrive at the spectrometer, which will be read as less absorption, i.e. a negative feature.

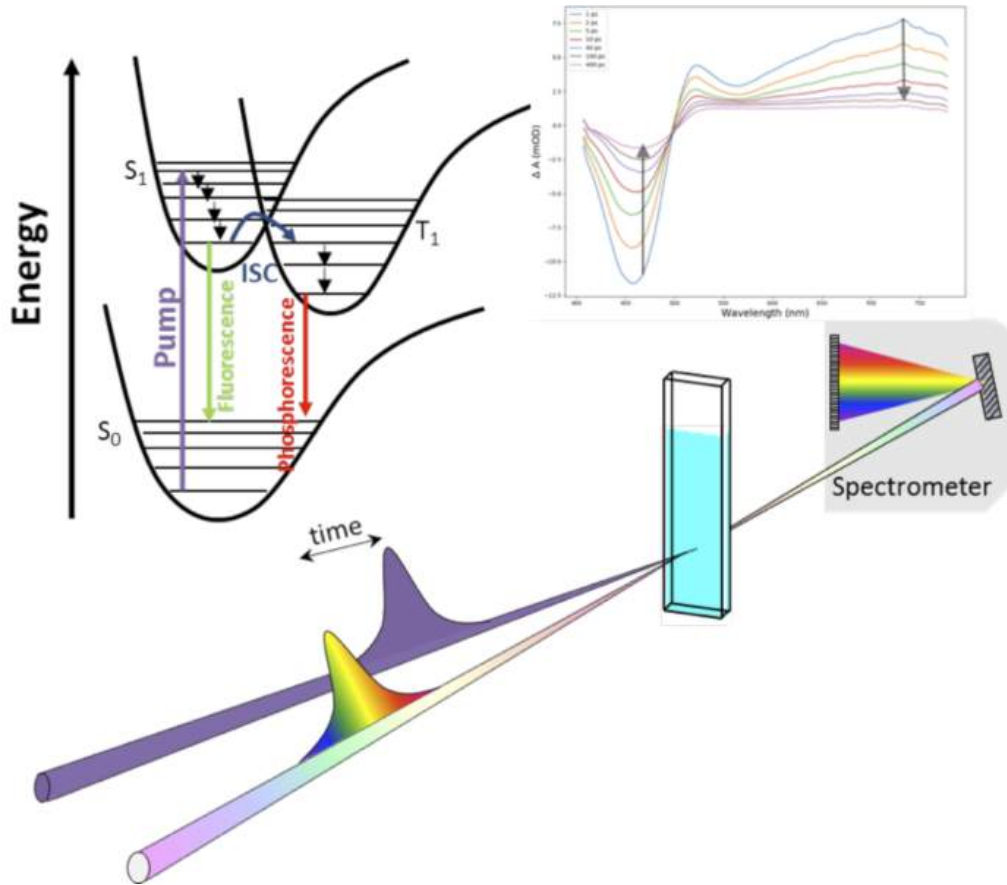


Figure 2.7: A simplified visual of TA operation. Inset left: Energy level diagram of possible transitions. Inset right: A corresponding spectral graph of ΔA vs wavelength. The change in time is shown by color in the lines, and additionally illustrated using arrows. Reproduced from [7].

decays occur. For example, if a ground state bleach feature and positive feature decay have the same lifetime, it is often reasonable to assume these refer to different aspects of the same process. Excitons decaying back into the ground state would cause a decrease in strength for both their absorbance signal and the ground state bleach.

The decay lifetime can be translated into an exciton diffusion length. From TA and other literature, the exciton diffusion length in P3HT:PCBM is determined to be on the order of 10nm.[9] Further examples of isolating P3HT:PCBM solar cell features through transient absorption spectroscopy are illustrated in the following section.

2.3.3 Relevant TA examples: Guo et al, (2009) and (2010)

Features can be identified in TA spectra primarily by sufficient experimentation to isolate the signal, good agreement with theory, or secondarily by agreement with existing literature. An expected feature is the ground state bleach aligning with the materials' steady-state (or ground-state) absorption.

As seen in the P3HT steady-state absorption spectrum (Figure 2.5a), three absorption

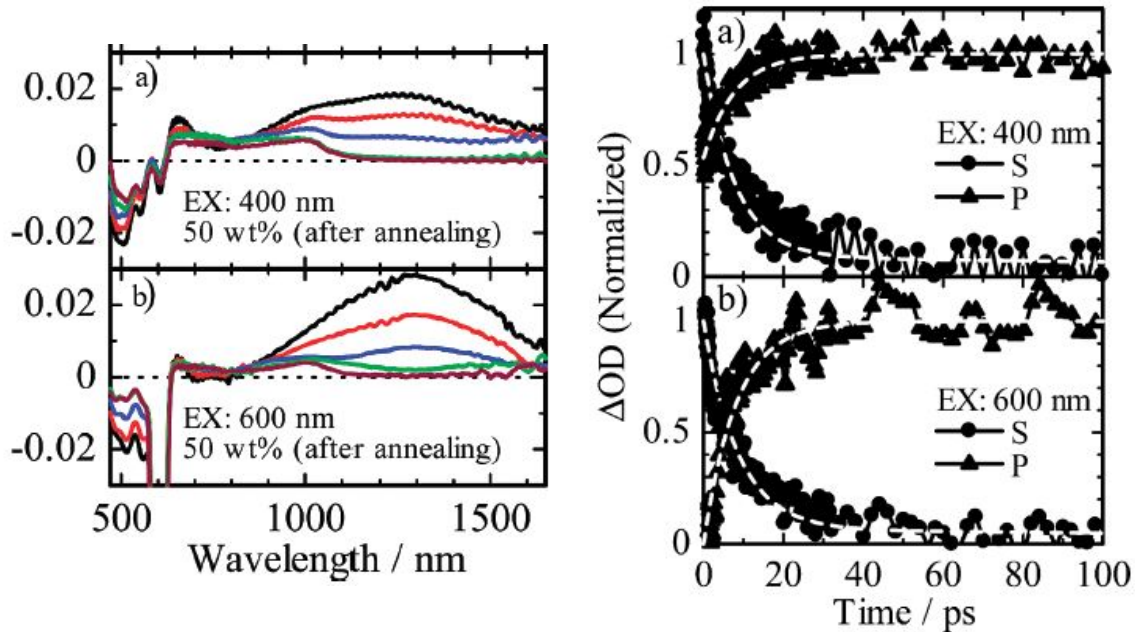


Figure 2.8: (left) TA Spectral graph for P3HT:PCBM BHJ films excited by (a) 400nm pump laser and (b) 600nm pump laser. (right) TA kinetics graph showing singlet exciton signal (*S*) taken at 1200nm, and polaron signal (*P*) taken at 1000nm after removing overlapping exciton signal. Pump laser (excitation) wavelength is (a) 400nm or (b) 600nm. Both reproduced from [4] with permission from the author.

peaks occur around 500, 560, and 610nm. These peaks are additionally seen as negative features in the ground state bleach. In Figures 2.5b and 2.8 (left), the peaks, now negative, are seen at these same wavelengths. One can expect the GSB to look approximately like a negative version of the steady-state absorption. The GSB spectrum in the figures are slightly different, owing to the narrowing of P3HT peaks when subject to TA spectroscopy.[64]

Other than the GSB, two main positive features are observed in data from Guo et al (2009) spectra for neat P3HT shown in Figure 2.5b – peaks around 700nm and 1250nm. The P3HT exciton is known from previous experiments to occur quite broadly with a peak around 1250nm.[64] The 700nm feature is the result of charge generation in P3HT. This can occur as the result of **exciton-exciton annihilation** – that is, when two excitons collide, it can enable the formation of a positive and negative charge within P3HT alone.[64] These states often recombine geminately, meaning the positive and negative charges generated from the same event will recombine with one another due to their Coulombic attraction.

The addition of PCBM (Figure 2.8(left)) creates a broad excitation between 700 and 1000nm, which is associated with P3HT:PCBM charge transfer. Free polarons in P3HT are expected to present a peak around 700nm; the paired polaron signature is a new signal around 1000nm.[4] Guo et al (2010) also note an increasing third feature around 800nm, which occurs much more commonly in regio-random P3HT films. Therefore, they attribute it to paired polarons in amorphously organized regions.[4]

To use the 1000nm feature to track the rise in paired polarons, a part of the 1000nm

signal which arises from the broad P3HT exciton feature (900-1600nm) must be removed. The isolated decay of P3HT exciton's peak near 1250nm serves as a basis for the exciton's contribution to the 1000nm feature. By normalizing both the 1000nm and 1250nm feature and subtracting, Guo et al (2010) are able to observe the paired polaron in isolation. They note the kinetic trace of both signals over the first 100ps, shown in Figure 2.8(right). Independent of pump excitation wavelength, both features decay with the same time period – the polaron (P) increasing, and the exciton (labelled S in the figure) decreasing. The trace strongly suggests that, during this time-frame, excitons are diffusing to the interface, and being converted into paired polarons.¹¹ Further results of several TA studies relating to P3HT:PCBM are presented in Table 2.3.

Selected TA Studies of P3HT and P3HT:PCBM films			
Paper	Guo et al 2010[4]	Tamai et al 2014[66]	Clafton et al 2013[8]
Type	BHJ film, annealed	Neat cP3HT films	NP blend solution
Features: <i>P3HT exciton</i>	1200 nm	1200 nm - 1300 nm	1250nm
<i>Free Polaron</i>	700 nm	—	—
<i>Paired Polaron</i>	1000 nm	—	1000nm
<i>Amorphous polaron</i>	850 nm	—	—
<i>Ground State Bleach</i>	480nm-610nm	450-600 nm	<610nm
Time constant: <i>P3HT exciton decay</i>	330 ps		200 ps
Other notes:	53% of polarons generated rapidly @400nm excitation, 0% @600nm excitation	20nm P3HT exciton diffusion length	

Table 2.3: A summary of several papers performing TA spectroscopy on P3HT:PCBM. Feature peaks and their assigned phenomena are listed.

2.3.4 Existing Nanoparticle TA

Only two studies appear to exist that perform TA spectroscopy on P3HT:PCBM nanoparticles.[8][48] This fact is somewhat surprising, given the effort to discern why NP solar cells lack the efficiency achievable by BHJ cells. TA spectroscopy can be used to determine if there are fundamental issues in NP cells with aspects like charge generation, charge mobility, and exciton diffusion.

¹¹The primary difference in the 400nm excitation is the very rapid (<100 fs) formation of charges. Since 600nm is just below P3HT's ground state transition energy, fast charge formation in the amorphous, intermixed region cannot occur. This process is also depicted in Figure 1.4.

Existing Findings

Clafton et al (2013) used TA spectroscopy to look at such nanoparticles in solution.[8] Curiously, they used tetrahydrofuran (THF) – a solvent almost exclusively employed in the nanoprecipitation process in the literature[9] – to create P3HT:PCBM nanoparticles via miniemulsion. Varying concentrations of PCBM relative to P3HT were used (0%, 5%, 20%, and 50%). Because of the unusual solvent, it may not be entirely clear if the resulting NPs had a core-shell morphology. Clafton et al (2013) showed that the charges produced in P3HT appear to dissociate roughly independently of PCBM concentration over the picosecond time scale – higher concentrations of PCBM only caused a higher retention of charge over 100ps-1ns timescales. This would be consistent with the generation of longer lived charges due to charge transfer in the NPs in solution.[8] Schwarz et al (2015) performed transient absorption spectroscopy on P3HT:PCBM nanoparticles created separately via miniemulsion and nanoprecipitation. P3HT and P3HT:PCBM nanoparticles were created under both methods – TA was performed on the NPs in solution. The paper’s main result is that cP3HT regions are produced in both types of nanoparticle – more predominantly in miniemulsion nanoparticles.[48]

Both studies viewed NP inks in DI water solution. However, no literature appears to have looked at NPs after annealing. Annealing is a crucial step in the formation of a NP solar cell’s active layer. Such an experiment may offer better insights into the underlying charge creation process and overall structure. Annealed NP films remain to be explored via TA spectroscopy.

2.4 Developed Goal

This dissertation aims to use transient absorption spectroscopy to observe and compare exciton and charge transfer dynamics in P3HT:PCBM nanoparticle film cells. Comparisons will be made with P3HT:PCBM nanoparticles in solution, as well as control bulk heterojunction films.

Chapter 3

Methodology

To achieve the desired goal under time constraints and lab restrictions due to Covid, it was decided the nanoparticle ink cells would independently formulated at the University of Sheffield. Once produced, their function as a solar cells would be discerned prior to performing transient absorption spectroscopy.

3.1 Summary

Nanoparticle inks were produced from the process given in Marks et al (2019), including the rapid evaporation step.[5] After the first run, Dr. Holmes (second author on the Marks paper) shared a similar protocol used in her lab for the production of nanoparticle inks, which was followed for future runs.[67] Rapid evaporation was replaced with a slower evaporation step. Active layers were spin-coated and annealed on quartz glass substrate to perform TA spectroscopy. Nanoparticle films were encapsulated in a glovebox using a cover glass and epoxy.

Prior to mounting in the Helios transient absorption spectrometer, all samples' steady-state absorbances in the UV-Vis were measured using a Cary60 spectrometer. To perform the necessary spectroscopy, solutions were diluted in a quartz glass cuvette with an appropriate amount of solvent to give an absorption of ≈ 0.2 OD at 400nm (the pump laser's excitation wavelength). In the case of films (primarily due to layer size), the absorbances could not be controlled. However, film thicknesses were appropriate to an active layer in a solar cell, thus absorption values were roughly around 0.2 OD. The absorption values were used to discern the energy absorbed per pump pulse.

Samples were aligned in a transient absorption (TA) spectrometer using the magic angle.¹ Recordings of the pump laser power were taken from the ThorLabs PM100D power meter with a silicon photodiode. The pump power was measured prior to a run then re-checked after the run to confirm the laser's stability.

TA analysis was performed using the native Helios software – time scales were chosen based on observation of the signal length. Time zero was chosen based on the earliest sign of any signal. Pre-processing of the data was performed in SurfaceXplorer; graphs were generated in Python.

¹ $\approx 54.74^\circ$ difference in polarization between the pump and probe lasers. This is the polarization relationship between the pump and probe which minimizes artefacts.

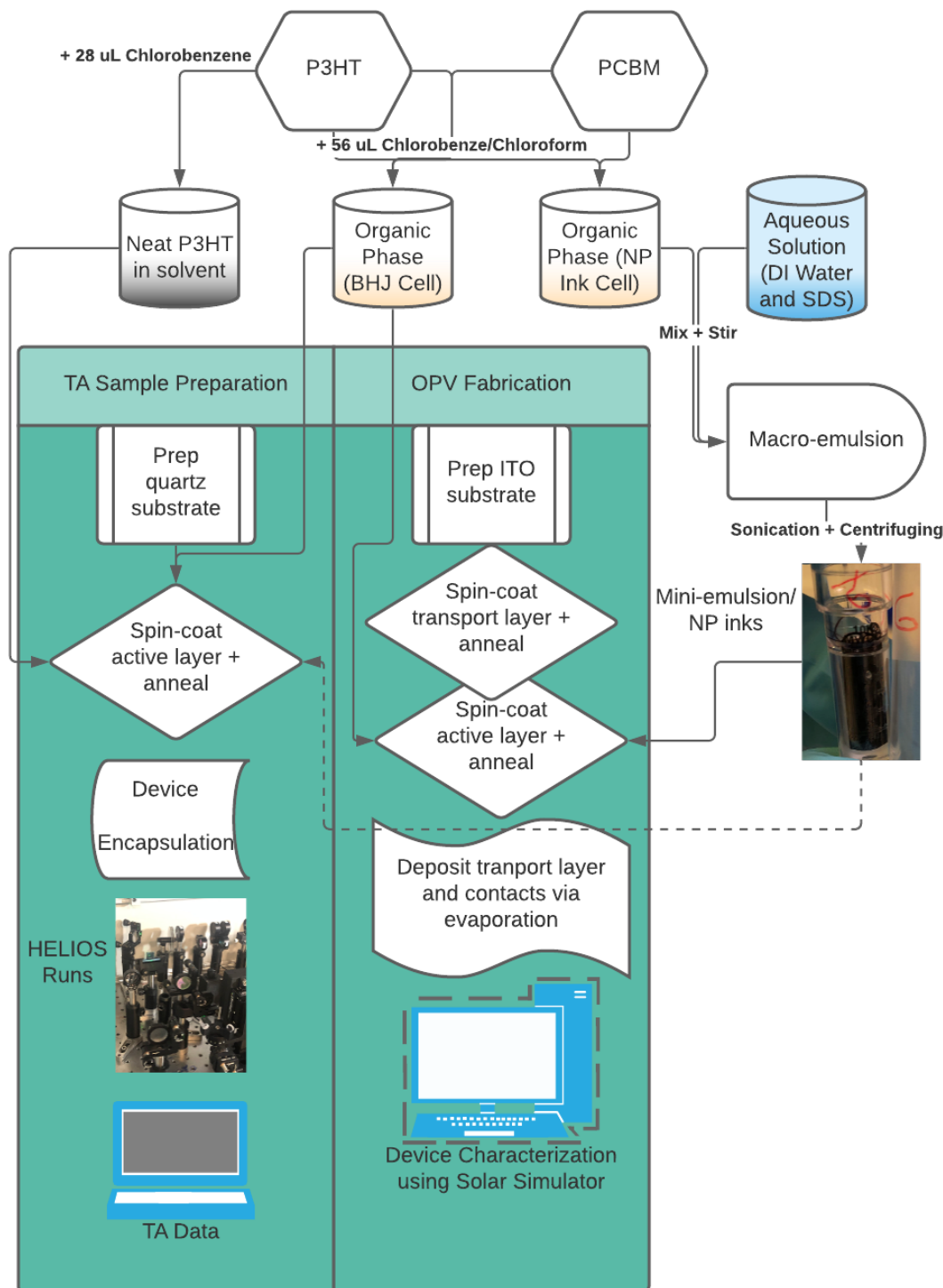


Figure 3.1: Diagram illustrating the different pathways followed in the experiments. Followed to completion, this produced two sets of working solar cells (BHJ and NP films) and three sets of optical film samples for TA analysis (neat P3HT, BHJ, and NP).

3.2 Material Preparations

3.2.1 Solutions

Solutions were produced in the clean lab (Hicks Building C6). The organic phase served as the basis of an active layer of a BHJ solar cell. Organic phase was also diluted in solution in a quartz cuvette (Hellma Macro, 2mm) to look at the absorption properties of the molecules in effective isolation from one another.

P3HT:PCBM Organic Phase

PC₇₀BM (Mw:1,031) powder was acquired from Ossilla and P3HT powder was acquired from Lisicon (Mw:74,000 and 97.3% regio-regularity).

To produce the organic phase, 15mg of P3HT and 15mg of PCBM were mixed into .56mL of solvent. For BHJ cells, the solvent was chlorobenzene; for NP inks, solvent was chloroform. Both were stirred with a magnetic stirrer to ensure mixing. For neat P3HT, 15mg of P3HT was dissolved into .28mL of chlorobenzene and stirred.

Water-based P3HT:PCBM Nanoparticles

Nanoparticle inks were formed by mixing an organic phase with an aqueous phase consistent with Marks et al (2019).[5] The organic P3HT:PCBM phase was produced as indicated in the prior section. After mixing (35°C, 500rpm for 25 minutes), the organic phase vial was placed into an ultrasonic bath for 25 minutes.

The aqueous phase was mixed from 2.78 mL of deionized (DI) water and 33mg of sodium dodecyl sulfate (SDS). Magnetic stirring at 500rpm was performed on the aqueous phase.

The organic phase was permitted to cool to prevent the escape of chloroform. The aqueous phase was gently added to the organic phase. Stirring and heating were again performed (33°C, 1100rpm for 1 hour) to generate the macroemulsion. The macroemulsion was then transferred to a biology lab (Firth Hall) for more powerful sonication.

To create the miniemulsion, the macroemulsion was sonicated in an ice bath for 2 minutes at 200W of power using a Fisherbrand Model 505 Sonic Dismembrator sonicator with a 7mm tip. Immediately after sonication, the miniemulsion was transferred to a pre-warmed hotplate at 60°C. The ink was stirred at 1200rpm under heat for three hours to facilitate solvent evaporation.²

Initially, centrifuging was performed using the large Sorvall ST16R centrifuge in the bio lab. By the third run (see 3.3) of this process, a smaller SciStir Micro centrifuge was lent out to the physics lab. This allowed for more control over the unbound SDS concentration in the water prior to spin-coating. DI water and surfactant were passed through Merck Millipore 10kDa filters, which filtered the nanoparticles.

²In the initial run, this step was done quickly in a rotary evaporator based on the procedure outlined in Marks et al (2019). However, Dr. Holmes indicated that the slower evaporation method was preferable.[67]

3.2.2 Films

OPV production

An indium-tin oxide (ITO) substrate produced by Ossilla was first cleaned using a combination of Hellmanex, isopropyl alcohol, and DI water. After this cleaning, the substrates were further prepared by 15 minutes of exposure in a UV-Ozone device.

For BHJ cells, the clean substrate was spin-coated with PEDOT:PSS. 40 μ L was deposited and spun at 6000rpm for 30s using an Ossila Spin-Coater inside a glovebox. After annealing (15 minutes @ 110°), the active layer was deposited dynamically. The organic phase P3HT:PCBM was spin-coated (dynamic, 30 μ L, 2000rpm, 40s). To test annealing conditions, the substrates were each heated for 10 minutes and were separately subject to chlorobenzene vapor exposure in varying order. The groups were: (1) 120°C anneal, no solvent vapor, (2) 150°C anneal, then solvent vapor, (3) solvent vapor, then 150°C anneal. After this, the substrates were transferred into an Angstrom thermal evaporator. The evaporator added charge-transport and metal contact layers of precise thickness. The electron-transport layer was lithium fluoride (1nm); the metal contacts were aluminium (100nm).

Because of the difficulties in spin-coating the NP ink cells (see Section 3.3 below), an ‘inverted stack’ layering was performed to produce NP film cells. The newly cleaned ITO substrates were first layered uniformly with zinc oxide (ZnO). After drying, an active layer of NP inks were spin-coated (dynamic, 20 μ L, 3000rpm, 20s) atop it. Because of the presence of water, a separate spin-coater outside the glovebox was used. The NP ink active layers were annealed for 10 minutes at 150°C. Then a hole-transport layer of MoO₃ (10nm) and silver (100nm) were thermally evaporated atop the active layer.

All devices were characterized by performing JV sweeps (0 to 1.2V, forward and reverse) in a Newport Solar Simulator (1 sun) with an Ossila S2006 I-V Test System.

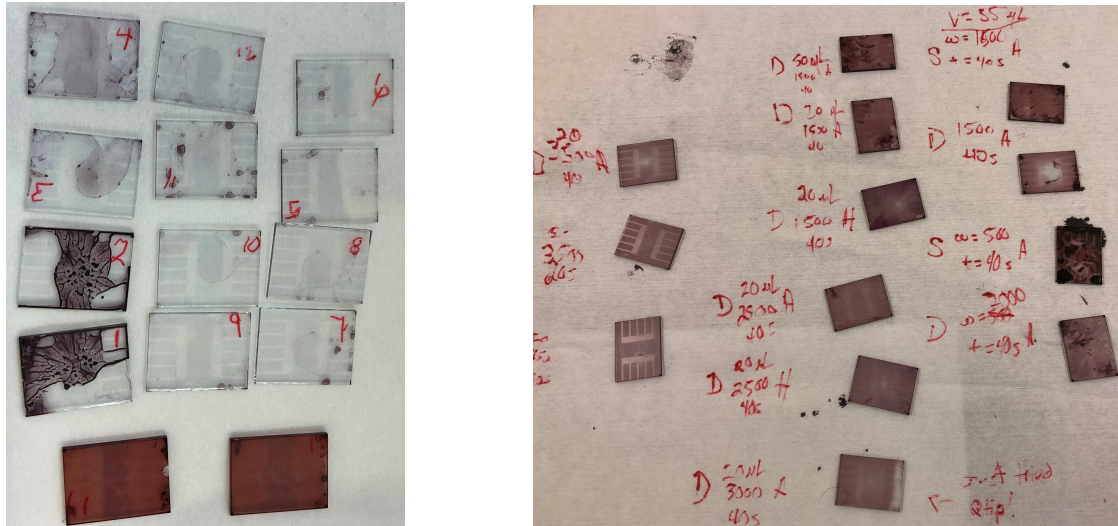
Optical sample production

The conditions for spin-coating and annealing the active layer in OPV cells were replicated on blank quartz glass substrate that had been cleaned similarly (using Hellmanex, DI, IPA, and 15 minutes in an UV-Ozone device). The first run of TA was performed on neat P3HT and conventional BHJ active layers. These films were not encapsulated. Once the importance of film encapsulation had been established, NP active layers on quartz substrate were encapsulated. However, several days had passed between drawer storage and encapsulation.

3.3 NP Ink Adjustments

While forming the nanoparticles was achieved, getting an ink that would properly spin coat and leave behind a uniform layer proved challenging. As shown in Figure 3.2a, the inks in the first run had difficulty layering onto a substrate. Of the substrates where any ink was left behind, aggregates are a clear issue. This proved to be the case as well in the second run. The third showed some improvement, as the centrifuge step was moved over to the clean lab (Hicks C6) where the spin-coating was performed. This allowed for some experimentation with the concentration of free surfactant. For these runs, the procedure outlined by Marks et al (2019), further expanded upon by Dr. Holmes was followed where possible.[67] The

incomparable sizes of the centrifuges used meant some guesswork was involved in the dialysis steps.



(a) Substrates annealing on a hotplate following spin-coating with first-run nanoparticle inks. The two finely-layered substrates on the bottom were standard bulk heterojunction P3HT:PCBM cells for comparison.

(b) Substrates spin coated with >6-month-old inks. Different volumes of ink, rotational speeds, and spin times were used.

Figure 3.2: Images of the NP film cells created in (a) Run 1 and (b) using old inks prior to Run 4.

Fortunately, some older inks³ were used to test spin-coating conditions ahead of the fourth run. The older inks were used to form an active layer, and it was observed that under short time, low volume, high speed dynamic spin-coating conditions (shown in figure 3.2b) the old inks produced more favorable films.

Another setback occurred when the old inks, while coating blank substrates admirably, failed to adequately coat cells using a filtered PEDOT:PSS layer. Researcher Emma Spooner suggested another attempt using a ZnO layer, i.e. inverted stack. The ZnO cells were more favorable for coating, resulting in functional cells with a peak efficiency of 0.1% (see Figure 4.2b). Though this PCE is low, it served to demonstrate that the old inks coated onto quartz glass functioned as the active layer of a solar cell. This validated performing transient absorption spectroscopy on the films.

The NP films were encapsulated using 22mm by 22mm Menzel-Glaser cover glasses and epoxy. David Bossanyi assisted in demonstrating the encapsulation procedure.

3.4 Spectroscopy

3.4.1 Ground (Steady) State Absorption

Solutions and films had their ultraviolet-visible (UV-Vis), Steady-State spectrum measured via the Cary60 in the Lord Porter lab prior to their use in the transient absorption spec-

³Originally from trial 2. The inks were left in a drawer for >6 months.

troscope and were measured again afterward⁴. While the spectra may be inconsistent due to different positioning of the films, care was taken to orient the films similarly. None of the films and solutions used showed any visual signs of degradation. Any differences in the steady-state spectra were attributable to reorienting the sample between runs in and out of the Helios setup.

3.4.2 TA Operation

A transient absorption (TA) spectroscope utilizes two lasers, a pump and a probe laser, to observe the sample when it is in an excited state.

The Helios setup and software were used for short timescale measurements (-5 to 7000 ps). For probe and pump lasers, a Spectra-Physics SPFIREF ACE-PA-40 and Time-Plate were used, respectively. Both were 40fs pulse at 10KHz frequency. The pump wavelength chosen was 400nm. The probe setup passed the laser through a non-linear optical medium, e.g. CaF or sapphire crystal, to generate a full spectrum of light. The UV-Vis and near infrared (NIR) were two light spectra attainable with such crystals.

3.4.3 Analysis

Assigning t_0

Care was taken to set time zero (t_0), which was taken as the initiation of overlap between the probe and pulse signal. When recording data, a progressive set of data points were chosen, meaning the computer moved the delay stage with the smallest Δt between data points occurring immediately after t_0 , and subsequently larger Δts occurring between data points further from t_0 . Sweeps were bidirectional, meaning data were taken by both increasing and decreasing the pump laser delay.

Different assignments of t_0 can add complications in comparing values to literature, as different definitions are used. The increase from initial signal to peak signal occurs on the order of 100s of femtoseconds. The spectra at 1ps were used to compare data, as it would not vary tremendously from its own peak and other peak signals in the literature.

Software

Data were pre-processed using SurfaceXplorer software.⁵ The pre-processed data were then loaded into Python (via Google Colab). The specific algorithms used, as well as the revisions, can be tracked via the link given in the present line.

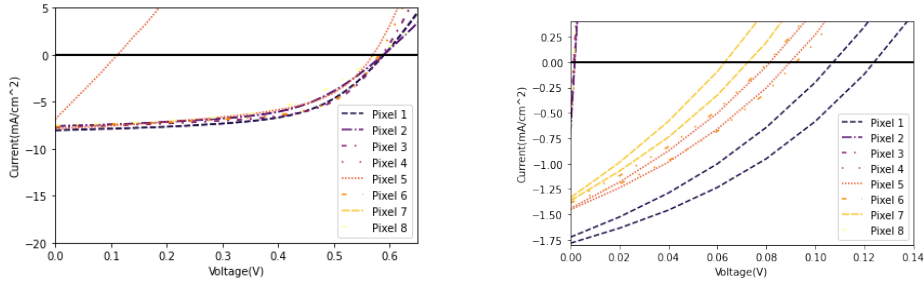
⁴This checked for degradation of the samples.

⁵Cropping, eliminating sets with missing values, background spectrum subtraction, and chirp correction.

Chapter 4

Results

4.1 OPV Results



(a) Sample JV sweeps for 8 pixels of one particular P3HT:PCBM BHJ solar cell. (b) Sample JV sweeps for 8 pixels of one particular P3HT:PCBM NP film solar cell.

Figure 4.1: Sample JV sweeps of both types of P3HT:PCBM solar cell – (a) BHJ and (b) NP. Although tested from 0-1.2V, the graphs scales are adjusted to better observe V_{OC} and J_{SC} .

To establish their function as solar cells, 8 components (pixels) of individual BHJ and NP cells were run in the I-V Test System referenced in Chapter 3. (See Figure 4.1.) A ‘forward’ and ‘reverse’ voltage sweep was performed for each pixel. V_{OC} and J_{SC} are visible as the x- and y-intercepts, respectively. Several individual pixel sweeps in Figure 4.1 appear as straight lines rather than curves. A linear result means at that location in the solar cell, the cell is functioning solely as a resistor and not generating current. These ‘dead pixels’ were removed in the final analysis.

The results presented in Table 4.1 indicate that the P3HT:PCBM bulk heterojunction cells had average efficiencies of about 1.7%, 2.5%, or 2.6%, depending on the annealing process used. The ‘solvent’ process referenced in Table 4.1 involved allowing the cell to sit in a container with chlorobenzene vapor.

The P3HT:PCBM nanoparticle cells had an average PCE of 0.03% over three working cells. The NP film cells, while functioning, performed far worse than BHJ cells. The low average PCE of the NP film cell was more characteristic of ‘as-cast’ NP cells in the literature.[44][41] Such cells are spin-coated, but not annealed.

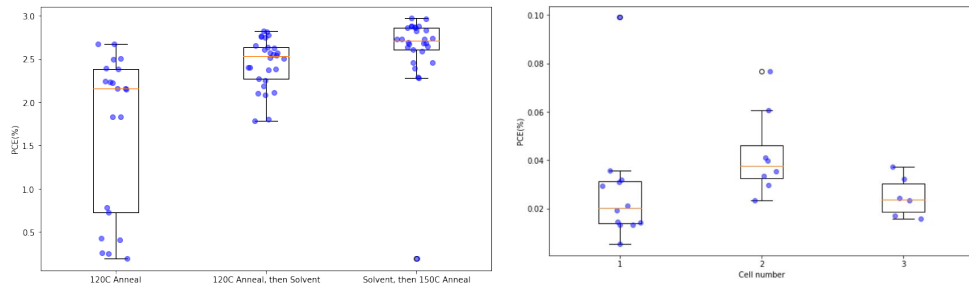
	J_{SC} (mA/cm ²)	V_{OC} (V)	P_{max} (mW/cm ²)	FF	PCE (%)
120C Anneal	-6.92 (+/- 0.85)	0.47 (+/- 0.18)	-1.65 (+/- 0.92)	0.45 (+/- 0.13)	1.67 (+/- 0.92)
120C Anneal, then Solvent	-7.53 (+/- 0.28)	0.58 (+/- 0.02)	-2.43 (+/- 0.29)	0.56 (+/- 0.07)	2.45 (+/- 0.29)
Solvent, then 150C Anneal	-7.83 (+/- 0.32)	0.56 (+/- 0.09)	-2.59 (+/- 0.5)	0.57 (+/- 0.07)	2.61 (+/- 0.51)

Table 4.1: Average values (and standard deviations) of useful solar cell quantities in BHJ film solar cells. Three groups were formed based on different annealing conditions.

	J_{SC} (mA/cm ²)	V_{OC} (V)	P_{max} (mW/cm ²)	FF	PCE (%)
All NP films	-1.51 (+/- 0.13)	0.07 (+/- 0.03)	-0.03 (+/- 0.02)	0.28 (+/- 0.04)	0.03 (+/- 0.02)

Table 4.2: Average values (and standard deviations) of useful solar cell quantities in NP film solar cells. Three individual cells were used, but nominally represent the same formation conditions.

In Figure 4.2, cell efficiencies are grouped by annealing process for BHJ films, or by individual cell number for NP films. All of the NP film cells were produced from the older inks using the same method. Each blue circle represents a PCE generated from an individual sweep (either forward or reverse). Other than the cell number or process, variation in the x-axis is meaningless and was performed to prevent crowding the data. The top performing cell for BHJ films had a PCE of 2.9%, whereas the top NP film had a PCE of 0.1%.



(a) Boxplot of BHJ film PCEs, annealed using three different processes.

(b) Boxplot of NP film PCEs, broken into individual cells. All cells are nominally the same.

Figure 4.2: Boxplots demonstrating the PCE values achieved in each run of the (a) BHJ and (b) NP ink cells. Each blue dot represents a PCE for a given run. Note: The ‘forward’ and ‘reverse’ components of the sweep were counted as individual runs.

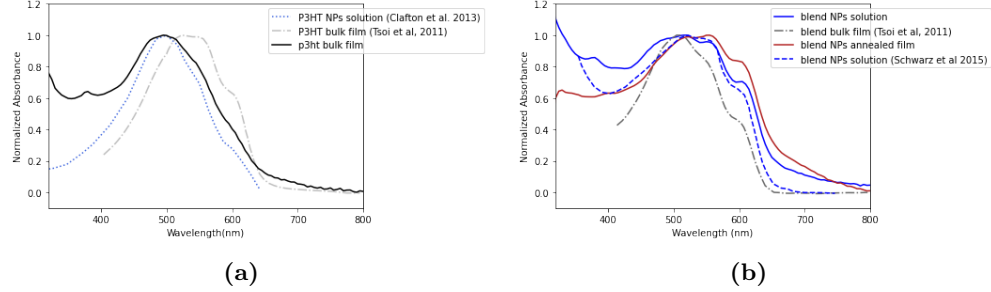


Figure 4.3: Steady-state spectra of different forms of (a) neat P3HT and (b) P3HT:PCBM blends in the UV-Visible (UV-Vis) region of the spectrum. Spectra shown in dotted lines are drawn from literature sources.[4]

4.2 Spectroscopy

4.2.1 Steady-state Spectra

P3HT is responsible for most of the absorption features in P3HT:PCBM blends. Two main forms of P3HT contribute to the spectrum – (1) aggregated, i.e. P3HT that forms a regular, collective, crystalline structure, and (2) amorphous. The h-aggregate model for P3HT nanoparticles has peaks at 500, 560, and 610nm.[48] For the bulk P3HT film created here (shown in Figure 4.3a), a significant blue shift is noticed compared to the literature spectrum. This shift, combined with less prominence in the aggregate peaks, suggest a greater proportion of amorphous P3HT in the film.

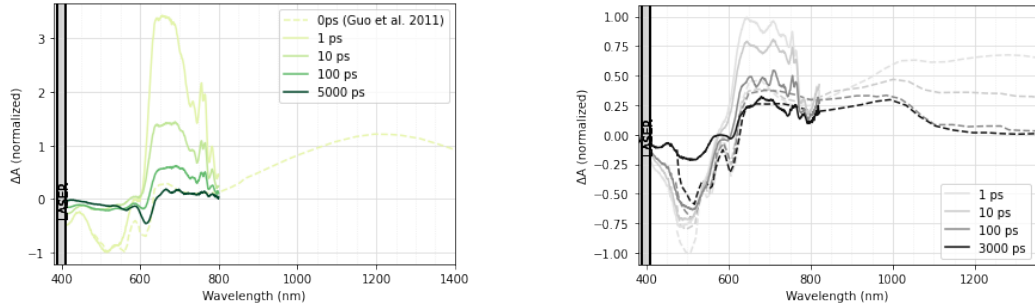
In Figure 4.3b, different P3HT:PCBM blend spectra are compared. The NP solution was close to the literature values. It is noted that the same h-aggregate peaks are observed in all blends, with some red shifting for nanoparticle blends. The different tails (around 700nm) suggest different amounts of light scattering in the samples. If adjusted for scattering, an increase in the 610nm peak in NP blends would still be observed. Increased prominence in the 560nm peak is also noticed for the annealed film. This feature is consistent with the annealing of the nanoparticles, which leads to more crystalline (aggregated) regions.

4.2.2 TA Spectra

In Figure 4.4a, GSB peaks for neat P3HT were broader and slightly blueshifted compared to Guo et al.[68] These features agree with the steady-state spectra and can be again explained by a greater proportion of amorphous P3HT.

The NIR spectrum was not taken for P3HT BHJ film and P3HT:PCBM BHJ film. Therefore, the NIR portions are supplemented by literature values from Guo et al. [68] (dashed). As discussed in 2.3.3, the positive feature observed due to TA is a P3HT free polaron, visible broadly from 650 to 750 nm. This feature is far stronger compared to literature and can also be seen to extend into and interfere with the ground state bleach signal around 610nm in Figure 4.4a.

Two differences noted between the charge state shown in TA and the Guo et al. (2010) [4] data) are the signal strength and wavelength. A much stronger charge signal relative to the ground state bleach is observed, which was possibly a consequence of the higher pump



(a) TA spectrum for Neat P3HT film. The data are presented against 0ps peak spectrum from Guo et al. [4], which includes near infrared (NIR) component.

(b) TA spectra for P3HT:PCBM BHJ films. Data is compared to Guo et al. [4] (dashed lines, time stamps the same by shade)

Figure 4.4: TA Spectra for (a) neat P3HT and (b) BHJ film. The pump energies for both were estimated as $90\mu\text{J}/\text{cm}^2$ per pulse.

strength. This increase in pump strength (at least two orders of magnitude) made exciton-exciton collisions more likely, generating free charges in neat P3HT. In terms of the spectral alignment, the data are more blueshifted in comparison to Guo et al (2010). The free polaron's intersection with the 610nm GSB feature would explain why that normally negative feature (as in [4]) begins as a positive feature. After the charges decay, the 610 nm feature returns to being a negative feature with the remaining ground state bleach.

For the BHJ blend film, the peaks occur at nearly the same wavelengths by 3000ps, but some time-dependent redshifting is observed that is not observed in Guo et al or generally in P3HT TA literature. The same pattern occurs at 610nm, where it begins positive and tends negative at later times. The data from 750-850nm becomes noisy owing to limitations in the spectrum from white light generation. In other words, towards the ends of the light spectrum there are fewer photons present and the TA probe is subsequently much more sensitive to small fluctuations, which lead to noisier data.

Differences in the charge generation with Guo et al. are again possible the result of different pump laser powers. By 3000ps, however, the signal strength of charge features are comparable. A main feature to keep in mind is the broad positive feature from 630-1020nm. This feature is assigned to charge states.¹

P3HT:PCBM nanoparticles in solution observe similar features to BHJ films, with several differences of note. Significantly greater strength is noticed in the GSB and peaks are narrower. The 610nm GSB feature is more clear, meaning the charge transfer feature is likely not as broad.

The portion of the UV-Vis data above 800nm and the NIR data below 850nm, representing the ends of probe light generation, are removed from the data. The amount of light generated in these regions is small, and therefore it is susceptible to minor changes in absorbance. The result is an increase in noise.

In the NIR, the broad charge transfer feature is observed as in Claftron et al [8], with two distinctions. A clear dip occurs around 950nm (see Figure 4.5a). This feature is not observed

¹Guo et al. [4] further isolates three aspects of the charge feature into part assignable to paired polarons, free polarons, and amorphous region polarons.

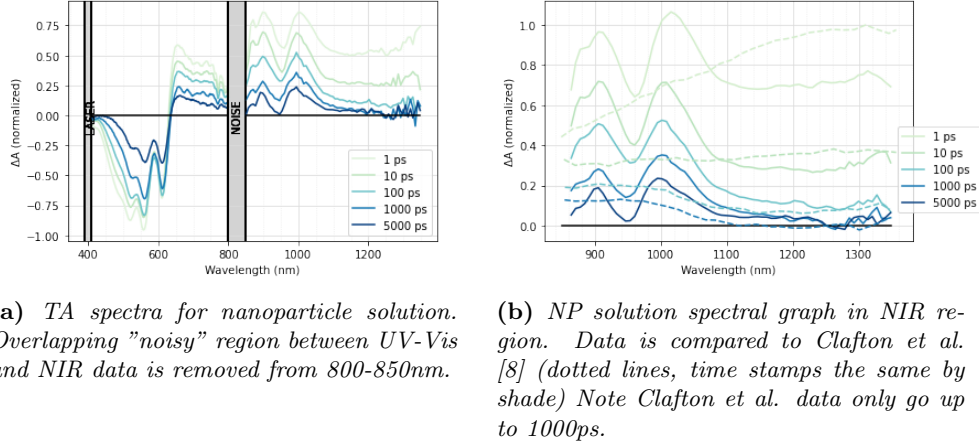


Figure 4.5: TA spectra for (a) nanoparticles in solution and (b) NP solution again, but focused in on the NIR region with comparison. Pump pulse energy is $130 \mu\text{J}/\text{cm}^2$ in NIR region, $60 \mu\text{J}/\text{cm}^2$ in UV-Vis region. For Claftron et al. pump pulse energy is $6.5 \mu\text{J}/\text{cm}^2$ [8]

by Claftron et al (2013). It may be an artefact due to saturation of the spectrometer around 950 nm (see Appendix A). If averaged, it may look similar to the charge generation feature from the bulk films. It is also possible that the paired polaron states are more prominent than P3HT exciton states when compared to Claftron et al (2013).[8] Further trials would be needed to distinguish if the dip is a feature or artefact.

The increased strength in the charge generation signal observed on early time scales can be assigned to additional signal from the P3HT exciton, which is more isolated around 1200nm. The P3HT exciton signal is almost fully quenched by 1000ps, consistent with the charge generation feature's improved alignment with the signal in the UV-Vis. Time scales are similar, with slightly faster exciton quenching observed in comparison to Claftron et al (2013).[8]

The NP film (Figure 4.6) spectra show sinusoidal patterns. These are a known effect (Fabry-Perot interference)[69] due to the encapsulated nature of the films.

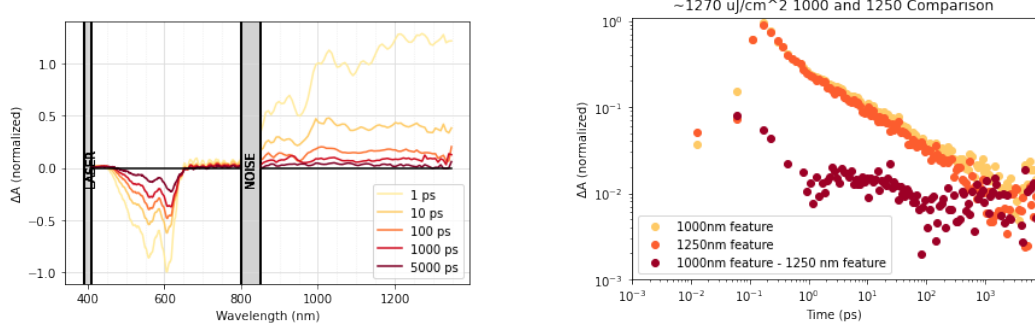
The GSB contains a more prominent 610nm peak and less GSB signatures at lower wavelengths. These observations are consistent with increased P3HT aggregation due to annealing.

The major difference in the NP film is the severe decrease in charge features. Any appearance of a charge signature between 650-1050nm may be the result of a broad P3HT exciton signal. Whether independent charge signals are discernible is further analyzed in the following section.

4.2.3 TA Kinetics

Kinetics graphs help clarify the dynamics of exciton and polaron features in the spectrum. The spectral graph in Figure 4.6 shows a positive feature at 1000nm – the peak wavelength associated with paired polarons. But, it is difficult to distinguish if this feature shows paired polarons, or is simply the extension of the broad P3HT exciton feature that peaks around 1250nm.

Figure 4.6b shows the dynamics of the (normalized) 1000nm feature subtracted from the



(a) TA Spectra for P3HT:PCBM NP film. Pump pulse energy is $130\mu\text{J}/\text{cm}^2$ in NIR region, $65\mu\text{J}/\text{cm}^2$ in UV-Vis region. NIR signal strength was reduced for continuity.

(b) Kinetics graph comparing the decay in NP film features at 1000nm (the paired polaron peak), 1250nm (the P3HT exciton peak), and the difference between them. Pump pulse energy is $1270\mu\text{J}/\text{cm}^2$. Scale is log-log.

Figure 4.6: Two graphs depicting TA spectroscopy data from the NP film. (a) A spectral graph, and (b) a kinetics graph.

1250nm feature. The resulting points are positive and, for times greater than 2ps, show a linear decrease on a log-log scale. This comparison helps establish some parts of the 1000nm feature did not occur purely from the broad P3HT exciton signal (1250nm).

In other words, there seem to be features of paired polarons. However, their signal is very slight – i.e. $\sim 1/100$ th of the total signal. These data also give a sense for what the paired polaron dynamics may look like in isolation from the P3HT exciton.

Notably, an increase in the paired polaron signal (1000nm) is not seen after removing the P3HT exciton (1250nm), as was the case in Guo et al (2010).[4] The rapidly decaying signal seems to suggest paired polarons are created almost instantly (~ 100 fs), rather than arising from exciton diffusion to the interface. Two explanations are explored in the Discussion.

Moving to Figure 4.7, it can be seen that the solution NPs are kinetically similar to the P3HT:PCBM BHJ cell in terms of free polaron generation (700nm peak). Around 675 nm (Figure 4.7a), the NP film is kinetically similar to the neat P3HT film. Charge generation in the NP film appears to occur only in the manner it is generated in P3HT without PCBM.

Increasing in wavelength (Figure 4.7b), the NP film begins to distinguish itself from neat P3HT by 750nm. Closer inspection shows this difference begins to arise around 700nm, which would be more consistent with the presence of a redder feature - either the amorphous or paired polaron, rather than the free polaron.

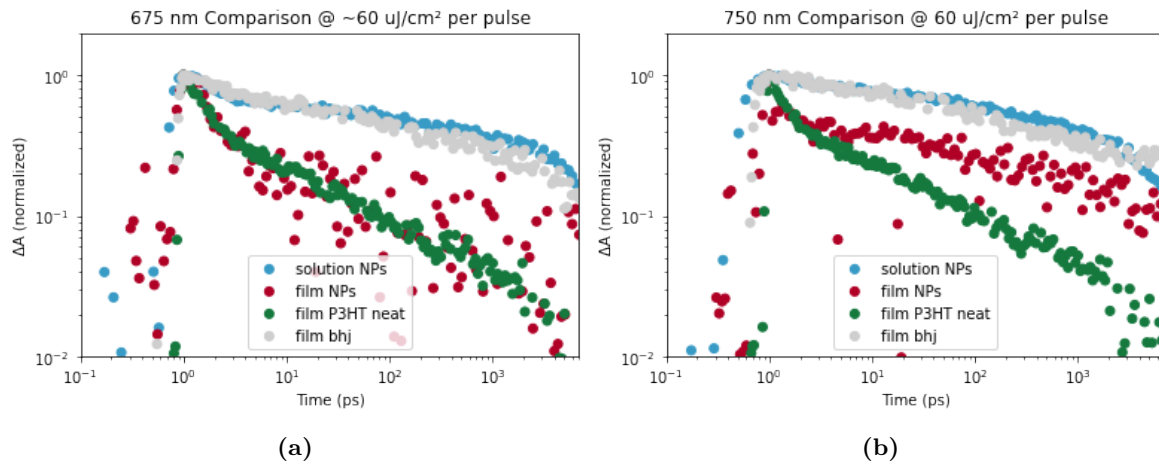


Figure 4.7: Kinetics scatterplots of features for all UV-Vis TA at (a) 675nm and (b) 750nm. The free polaron feature normally peaks around 700nm in P3HT:PCBM cells. Because the data were taken at different times, pump pulse energies are not quite the same, but all are on the order of $60\mu J/cm^2$. Scale is log-log.

Chapter 5

Discussion

The results show a lack of charge generation in the annealed NP films. Charge generation in the unannealed NP solution showed a charge lifetime comparable to its BHJ counterpart. Several features of the data ought be considered:

(1) *The lack of increasing charge features amongst NP films.*

At least some bound charges appear to have been formed in the NP films. So (1) seems to imply that most or all charges were generated within $\sim 100\text{fs}$. One possible explanation is that the film is fairly intermixed with P3HT and PCBM. The data from Figure 4.7a suggest this is not the case, however. In regards to free polaron generation, at least, the NP films behave similarly to cP3HT.

(2) *There are clear signs of crystalline P3HT in the NPs, in particular in film.*

Both the steady-state spectra and the GSB of the TA spectra seem to indicate an aggregated, crystalline portion of P3HT in the NPs. The overall lack of charge generation in NP films is also consistent with less inter-mixture.

An alternative explanation to largely intermixed NPs might lie in the high pump powers used for the NIR spectroscopy. At such high powers, exciton generation is frequent in the film. In films with P3HT, there is generally a fast-decaying charge component that arises from exciton-exciton (**e-e**) annihilation.[4]

The kinetics graphs in Figures 4.6b and 4.7 are given by two (and possibly more) time regimes. There is a faster decay dynamic¹ in the 100fs-1ps range, which is then dominated by a longer decay feature. The strength of the fast-decaying features ($\sim 1\text{ps}$) describe frequent exciton-exciton annihilation after the pump pulse. If enough excitons are being generated to make these collisions frequent, and the NP film's PCBM is fairly segregated from its P3HT, then perhaps the only excitons which are forming charge states are those in the immediate vicinity of the PCBM. Excitons not near the interface would then undergo e-e annihilation or eventual decay.

(3) *PCEs of the NP film are similar to that of unannealed NP films in literature.*

It seems unlikely the films were, in fact, similar to an unannealed NP ink. The NP film was subjected to a relatively high temperature and length of annealing. In the literature, this is more consistent with a NP film which is mainly phase-segregated.[56]

Although charge transport may additionally be an issue for the NP films, Figure 4.6 shows the dominant issue was the lack of charge generation. Charges that were generated

¹i.e. a steeper line.

in film at a high pump power ($\sim 1\text{mJ/pulse}$) were in the 1000nm/paired polaron domain. Charge is being generated, but it appears limited to paired or amorphous-region polarons. The start of an additional feature over neat P3HT in NP films around 700nm is consistent with Guo et al's global analysis assignment of the amorphous-region polaron. The limited charge formation, combined with the additional barrier of charge dissociation, explain some of the poor performance.

In total, the film formation process was harmful to charge generation. If the problem lies in the annealing, it contradicts several studies which note marked improvement in PCEs post-annealing.[5][9][52] For example, Vaughn et al gives a peak PCE of 0.05% for an as-cast film (i.e. spun from solution as the active layer with no additional processing). The peak PCE increased to 1.99% after 10 minutes annealing at 130° C.[41]

It should be noted that some studies have shown either a decrease after a certain amount of annealing time[41], or a general pattern of lower PCE with increased heating.[5] Due to the number of variables involved, the issue is confounded in the literature. Further annealing affects remain a possibility.

Literature review seems to suggest one issue of charge generation occurred as a result of open air exposure.[21] This mechanism is not well-understood. However, particular issues arising between the as-cast morphology and annealing cannot be overlooked. If the presence of surfactant played a role, it is unclear why most charge generation was suppressed here but gave PCEs of around 1% in Marks et al (2019).[5]

Due to the time pressures of the research, other methods of film characterization could not be pursued. Such methods could help rule out some possibilities and further clarify the charge generation issue. While further aspects of quantitative analysis in the TA spectroscopy data could be pursued (e.g. global analysis to separate out different sources of signal), it is better reserved for a similar project pursued with better controls and understanding.

Chapter 6

Conclusions

The data exhibit the limiting of charge generation in our nanoparticle films. The same ink which clearly produced charge states in solution did not observably produce charges as an annealed film. The solution appeared to have comparable charge generation properties to the BHJ film.

Annealing is a key process in determining the transfer of charges (and therefore PCE) in NP ink solar cells. But different experimental conditions confound the issue. The same ink used on the optical film for spectroscopy did produce functional solar cells. These cells, which were not encapsulated, did not appear to function after several days exposed to open air. Because it was unclear they would be needed, the annealed NP films on optical substrates were left in a substrate container for a few days before encapsulation. This would have exposed them to air, harming their function in generating charges.

If this is the case, then why and to what extent is open air exposure harming nanoparticle ink solar cells? If not, what is occurring in the deposition and annealing that harms charge generation?

Testing would involve the reliable production of nanoparticle solar cells allowing different resting times between annealing the nanoparticle ink films and encapsulation. Scale would be understood best by allowing a log-like time for resting (e.g. 1 minute, 1 hour, 1 day, 1 week). To further elucidate this process, as-cast (i.e. spin-coated, but not annealed) films should also be explored.

Pursued in conjunction with other controls and methods, TA can help isolate issues within the charge generation process. Our NP solution results seem to suggest more similarity with its BHJ counterparts than PCEs would suggest. A key hidden in the cell formation process may drastically improve organic nanoparticle ink solar cells, unlocking a door to cleaner forms of renewable energy.

Bibliography

- [1] Emma Spooner. Organic photovoltaics: An introduction. URL <https://www.ossila.com/pages/organic-photovoltaics-introduction>.
- [2] Ossila. P3ht. URL <https://www.ossila.com/products/p3ht>.
- [3] Marie D. M. Faure and Benoît H. Lessard. Layer-by-layer fabrication of organic photovoltaic devices: material selection and processing conditions. 9(1):14–40. ISSN 2050-7526, 2050-7534. doi: 10.1039/D0TC04146G. URL <http://xlink.rsc.org/?DOI=DOTC04146G>.
- [4] Jiamo Guo, Hideo Ohkita, Hiroaki Benten, and Shinzaburo Ito. Charge generation and recombination dynamics in poly(3-hexylthiophene)/fullerene blend films with different regioregularities and morphologies. 132(17):6154–6164, . ISSN 0002-7863, 1520-5126. doi: 10.1021/ja100302p. URL <https://pubs.acs.org/doi/10.1021/ja100302p>.
- [5] Melissa Marks, Natalie P. Holmes, Anirudh Sharma, Xun Pan, Riku Chowdhury, Matthew G. Barr, Coralie Fenn, Matthew J. Griffith, Krishna Feron, A. L. David Kilcoyne, David A. Lewis, Mats R. Andersson, Warwick J. Belcher, and Paul C. Dastoor. Building intermixed donor–acceptor architectures for water-processable organic photovoltaics. 21(10):5705–5715. ISSN 1463-9076, 1463-9084. doi: 10.1039/C8CP07137C. URL <http://xlink.rsc.org/?DOI=C8CP07137C>.
- [6] F Temps. Transient electronic absorption. URL <https://www.temps.phc.uni-kiel.de/en/research/laboratories-and-instrumentation/fs-transient-absorption>.
- [7] MKS Newport. Transient absorption spectrometer. URL <https://www.newport.com/f/transient-absorption-spectrometer>.
- [8] Scott N. Clafton, David M. Huang, William R. Massey, and Tak W. Kee. Femtosecond dynamics of excitons and hole-polarons in composite p3ht/PCBM nanoparticles. 117(16):4626–4633. ISSN 1520-6106, 1520-5207. doi: 10.1021/jp308876z. URL <https://pubs.acs.org/doi/10.1021/jp308876z>.
- [9] Alexandre Holmes, Elise Deniau, Christine Lartigau-Dagron, Antoine Bousquet, Sylvain Chambon, and Natalie P. Holmes. Review of waterborne organic semiconductor colloids for photovoltaics (pre-print). page acsnano.0c10161, . ISSN 1936-0851, 1936-086X. doi: 10.1021/acsnano.0c10161. URL <https://pubs.acs.org/doi/10.1021/acsnano.0c10161>. Pre-print.

- [10] David Dodman. Blaming cities for climate change? an analysis of urban green-house gas emissions inventories. 21(1):185–201. ISSN 0956-2478, 1746-0301. doi: 10.1177/0956247809103016. URL <http://journals.sagepub.com/doi/10.1177/0956247809103016>.
- [11] IEA. Greenhouse gas emissions from energy: Overview, . URL <https://www.iea.org/reports/greenhouse-gas-emissions-from-energy-overview>.
- [12] Climate change 2014: synthesis report.
- [13] IEA. Electricity, . URL <https://www.iea.org/reports/global-energy-review-2021/electricity>.
- [14] Fraunhofer ISE. Photovoltaics report. URL <http://www.ise.fraunhofer.de/en/downloads-englisch/pdf-files-englisch/photovoltaics-report-slides.pdf>.
- [15] Ewa Klugmann-Radziemska and Anna Kuczyńska-Łazewska. The use of recycled semi-conductor material in crystalline silicon photovoltaic modules production - a life cycle assessment of environmental impacts. 205:110259. ISSN 09270248. doi: 10.1016/j.solmat.2019.110259. URL <https://linkinghub.elsevier.com/retrieve/pii/S0927024819305884>.
- [16] Vincenzo Muteri, Maurizio Cellura, Domenico Curto, Vincenzo Franzitta, Sonia Longo, Marina Mistretta, and Maria Laura Parisi. Review on life cycle assessment of solar photovoltaic panels. 13(1):252. ISSN 1996-1073. doi: 10.3390/en13010252. URL <https://www.mdpi.com/1996-1073/13/1/252>.
- [17] Pengfei Zhao, Junwei Guo, Guanghui Yan, Guangqing Zhu, Xiangnan Zhu, Zhenxing Zhang, and Bo Zhang. A novel and efficient method for resources recycling in waste photovoltaic panels: High voltage pulse crushing. 257:120442. ISSN 09596526. doi: 10.1016/j.jclepro.2020.120442. URL <https://linkinghub.elsevier.com/retrieve/pii/S0959652620304893>.
- [18] Sanna-Mari Nevala, Joseph Hamuyuni, Tero Junnila, Tuomas Sirviö, Stefan Eisert, Benjamin P. Wilson, Rodrigo Serna-Guerrero, and Mari Lundström. Electro-hydraulic fragmentation vs conventional crushing of photovoltaic panels – impact on recycling. 87:43–50. ISSN 0956053X. doi: 10.1016/j.wasman.2019.01.039. URL <https://linkinghub.elsevier.com/retrieve/pii/S0956053X19300534>.
- [19] T. Arnold, C. M. Harth, J. Muhle, A. J. Manning, P. K. Salameh, J. Kim, D. J. Ivy, L. P. Steele, V. V. Petrenko, J. P. Severinghaus, D. Baggenstos, and R. F. Weiss. Nitrogen trifluoride global emissions estimated from updated atmospheric measurements. 110(6):2029–2034. ISSN 0027-8424, 1091-6490. doi: 10.1073/pnas.1212346110. URL <http://www.pnas.org/cgi/doi/10.1073/pnas.1212346110>.
- [20] JinkoSolar. JinkoSolar addresses environmental concerns related to its zhejiang jinko facility.

- [21] Jenny Nelson. Organic photovoltaic films. 6(1):87–95. ISSN 13590286. doi: 10.1016/S1359-0286(02)00006-2. URL <https://linkinghub.elsevier.com/retrieve/pii/S1359028602000062>.
- [22] Frederik C. Krebs, Suren A. Gevorgyan, and Jan Alstrup. A roll-to-roll process to flexible polymer solar cells: model studies, manufacture and operational stability studies. 19(30):5442. ISSN 0959-9428, 1364-5501. doi: 10.1039/b823001c. URL <http://xlink.rsc.org/?DOI=b823001c>.
- [23] Seth B. Darling and Fengqi You. The case for organic photovoltaics. 3(39):17633. ISSN 2046-2069. doi: 10.1039/c3ra42989j. URL <http://xlink.rsc.org/?DOI=c3ra42989j>.
- [24] P. R. Berger and M. Kim. Polymer solar cells: P3ht:PCBM and beyond. 10(1):013508. ISSN 1941-7012. doi: 10.1063/1.5012992. URL <http://aip.scitation.org/doi/10.1063/1.5012992>.
- [25] Ishan C Ghosekar and Ganesh C Patil. Review on performance analysis of p3ht:PCBM-based bulk heterojunction organic solar cells. 36(4):045005. ISSN 0268-1242, 1361-6641. doi: 10.1088/1361-6641/abe21b. URL <https://iopscience.iop.org/article/10.1088/1361-6641/abe21b>.
- [26] Hendrik C.Swart, Odireleng M. Ntwaeborwa, Pontsho S. Mbule, Mokhotjwa S. Dhlamini, and Bakang B.Mothudi. P3ht: PCBM based solar cells: A short review focusing on ZnO nanoparticles buffer layer, post-fabrication annealing and an inverted geometry. 5(2). ISSN 21616221, 21616221. doi: 10.17265/2161-6221/2015.1-2.002. URL <http://www.davidpublisher.org/index.php/Home/Article/index?id=10271.html>.
- [27] G. Yu and A. J. Heeger. Charge separation and photovoltaic conversion in polymer composites with internal donor/acceptor heterojunctions. 78(7):4510–4515. ISSN 0021-8979, 1089-7550. doi: 10.1063/1.359792. URL <http://aip.scitation.org/doi/10.1063/1.359792>.
- [28] K. Landfester, R. Montenegro, U. Scherf, R. Güntner, U. Asawapirom, S. Patil, D. Neher, and T. Kietzke. Semiconducting polymer nanospheres in aqueous dispersion prepared by a miniemulsion process. 14(9):651–655. ISSN 1521-4095. doi: 10.1002/1521-4095(20020503)14:9<651::AID-ADMA651>3.0.CO;2-V. URL <http://onlinelibrary.wiley.com/doi/abs/10.1002/1521-4095%2820020503%2914%3A9%3C651%3A%3AAID-ADMA651%3E3.0.CO%3B2-V>. eprint: <https://onlinelibrary.wiley.com/doi/pdf/10.1002/1521-4095%2820020503%2914%3A9%3C651%3A%3AAID-ADMA651%3E3.0.CO%3B2-V>.
- [29] Qishi Liu, Yufan Jiang, Ke Jin, Jianqiang Qin, Jingui Xu, Wenting Li, Ji Xiong, Jinfeng Liu, Zuo Xiao, Kuan Sun, Shangfeng Yang, Xiaotao Zhang, and Liming Ding. 18% efficiency organic solar cells. 65(4):272–275. ISSN 20959273. doi: 10.1016/j.scib.2020.01.001. URL <https://linkinghub.elsevier.com/retrieve/pii/S2095927320300013>.
- [30] Yong Cui, Ye Xu, Huifeng Yao, Pengqing Bi, Ling Hong, Jianqi Zhang, Yunfei Zu, Tao Zhang, Jinzhao Qin, Junzhen Ren, Zhihao Chen, Chang He, Xiaotao Hao, Zhixiang Wei, and Jianhui Hou. Single-junction organic photovoltaic cell with 19% efficiency.

- page 2102420. ISSN 0935-9648, 1521-4095. doi: 10.1002/adma.202102420. URL <https://onlinelibrary.wiley.com/doi/10.1002/adma.202102420>.
- [31] Chen Xie, Thomas Heumüller, Wolfgang Gruber, Xiaofeng Tang, Andrej Classen, Isabel Schuldes, Matthew Bidwell, Andreas Späth, Rainer H. Fink, Tobias Unruh, Iain McCulloch, Ning Li, and Christoph J. Brabec. Overcoming efficiency and stability limits in water-processing nanoparticulate organic photovoltaics by minimizing microstructure defects. 9(1):5335, . ISSN 2041-1723. doi: 10.1038/s41467-018-07807-5. URL <http://www.nature.com/articles/s41467-018-07807-5>.
 - [32] Lien D'Olieslaeger, Geert Pirotte, Ilaria Cardinaletti, Jan D'Haen, Jean Manca, Dirk Vanderzande, Wouter Maes, and Anitha Ethirajan. Eco-friendly fabrication of PB-DTTPD:PCT1bm solar cells reaching a PCE of 3.8% using water-based nanoparticle dispersions. 42:42–46. ISSN 15661199. doi: 10.1016/j.orgel.2016.12.018. URL <https://linkinghub.elsevier.com/retrieve/pii/S1566119916305523>.
 - [33] Su-Hwan Lee, Ji-Heon Kim, Tae-Hun Shim, and Jea-Gun Park. Effect of interface thickness on power conversion efficiency of polymer photovoltaic cells. 5(1):47–50. ISSN 17388090. doi: 10.3365/eml.2009.03.047. URL <http://link.springer.com/10.3365/eml.2009.03.047>.
 - [34] Timothy S. Gehan, Monojit Bag, Lawrence A. Renna, Xiaobo Shen, Dana D. Algaier, Paul M. Lahti, Thomas P. Russell, and Dhandapani Venkataraman. Multiscale active layer morphologies for organic photovoltaics through self-assembly of nanospheres. 14 (9):5238–5243. ISSN 1530-6984, 1530-6992. doi: 10.1021/nl502209s. URL <https://pubs.acs.org/doi/10.1021/nl502209s>.
 - [35] Monojit Bag, Timothy S. Gehan, Lawrence A. Renna, Dana D. Algaier, Paul M. Lahti, and D. Venkataraman. Fabrication conditions for efficient organic photovoltaic cells from aqueous dispersions of nanoparticles. 4(85):45325–45331. ISSN 2046-2069. doi: 10.1039/C4RA07463G. URL <http://xlink.rsc.org/?DOI=C4RA07463G>.
 - [36] C. W. Tang. Two-layer organic photovoltaic cell. 48(2):183–185. ISSN 0003-6951, 1077-3118. doi: 10.1063/1.96937. URL <http://aip.scitation.org/doi/10.1063/1.96937>.
 - [37] Julien Gorenflo, Andreas Paulke, Fortunato Piersimoni, Jannic Wolf, Zhipeng Kan, Federico Cruciani, Abdulrahman El Labban, Dieter Neher, Pierre M. Beaujuge, and Frédéric Laquai. From recombination dynamics to device performance: Quantifying the efficiency of exciton dissociation, charge separation, and extraction in bulk heterojunction solar cells with fluorine-substituted polymer donors. 8(4):1701678. ISSN 16146832. doi: 10.1002/aenm.201701678. URL <https://onlinelibrary.wiley.com/doi/10.1002/aenm.201701678>.
 - [38] Ian A. Howard and Frédéric Laquai. Optical probes of charge generation and recombination in bulk heterojunction organic solar cells. 211(19):2063–2070. ISSN 10221352. doi: 10.1002/macp.201000353. URL <https://onlinelibrary.wiley.com/doi/10.1002/macp.201000353>.

- [39] Chen Xie, Andrej Classen, Andreas Späth, Xiaofeng Tang, Jie Min, Markus Meyer, Chaohong Zhang, Ning Li, Andres Osvet, Rainer H. Fink, and Christoph J. Brabec. Overcoming microstructural limitations in water processed organic solar cells by engineering customized nanoparticulate inks. 8(13):1702857, . ISSN 16146832. doi: 10.1002/aenm.201702857. URL <https://onlinelibrary.wiley.com/doi/10.1002/aenm.201702857>.
- [40] Sylvain Chambon, Christophe Schatz, Vivien Sébire, Bertrand Pavageau, Guillaume Wantz, and Lionel Hirsch. Organic semiconductor core–shell nanoparticles designed through successive solvent displacements. 1(4):431–438. ISSN 2051-6347, 2051-6355. doi: 10.1039/C4MH00021H. URL <http://xlink.rsc.org/?DOI=C4MH00021H>.
- [41] Ben Vaughan, Andrew Stapleton, Elisa Sesa, Natalie P. Holmes, Xiaojing Zhou, Paul C. Dastoor, and Warwick J. Belcher. Engineering vertical morphology with nanoparticulate organic photovoltaic devices. 32:250–257. ISSN 15661199. doi: 10.1016/j.orgel.2016.02.022. URL <https://linkinghub.elsevier.com/retrieve/pii/S1566119916300660>.
- [42] Natalie P. Holmes, Melissa Marks, Pankaj Kumar, Renee Kroon, Matthew G. Barr, Nicolas Nicolaidis, Krishna Feron, Almantas Pivrikas, Adam Fahy, Amaia Diaz de Zerio Mendaza, A.L.David Kilcoyne, Christian Müller, Xiaojing Zhou, Mats R. Andersson, Paul C. Dastoor, and Warwick J. Belcher. Nano-pathways: Bridging the divide between water-processable nanoparticulate and bulk heterojunction organic photovoltaics. 19:495–510, . ISSN 22112855. doi: 10.1016/j.nanoen.2015.11.021. URL <https://linkinghub.elsevier.com/retrieve/pii/S221128551500453X>.
- [43] Fallon J. M. Colberts, Martijn M. Wienk, and René A. J. Janssen. Aqueous nanoparticle polymer solar cells: Effects of surfactant concentration and processing on device performance. 9(15):13380–13389. ISSN 1944-8244, 1944-8252. doi: 10.1021/acsami.7b00557. URL <https://pubs.acs.org/doi/10.1021/acsami.7b00557>.
- [44] Laurie Parrenin, Gildas Laurans, Eleni Pavlopoulou, Guillaume Fleury, Gilles Pecastaings, Cyril Brochon, Laurence Vignau, Georges Hadzioannou, and Eric Cloutet. Photoactive donor–acceptor composite nanoparticles dispersed in water. 33(6):1507–1515. ISSN 0743-7463, 1520-5827. doi: 10.1021/acs.langmuir.6b04496. URL <https://pubs.acs.org/doi/10.1021/acs.langmuir.6b04496>.
- [45] Natalie P. Holmes, Kerry B. Burke, Prakash Sista, Matthew Barr, Harsha D. Magurudeniya, Mihaela C. Stefan, A.L.David Kilcoyne, Xiaojing Zhou, Paul C. Dastoor, and Warwick J. Belcher. Nano-domain behaviour in p3ht:PCBM nanoparticles, relating material properties to morphological changes. 117:437–445, . ISSN 09270248. doi: 10.1016/j.solmat.2013.06.003. URL <https://linkinghub.elsevier.com/retrieve/pii/S0927024813002882>.
- [46] Furqan Almyahi, Thomas R. Andersen, Nathan Cooling, Natalie P. Holmes, Adam Fahy, Matthew G. Barr, David Kilcoyne, Warwick Belcher, and Paul C. Dastoor. Optimization, characterization and upscaling of aqueous solar nanoparticle inks for organic photovoltaics using low-cost donor:acceptor blend. 52:71–78. ISSN 15661199. doi: 10.1016/j.orgel.2017.10.008. URL <https://linkinghub.elsevier.com/retrieve/pii/S1566119917304986>.

- [47] Mohammed F. Al-Mudhaffer, Matthew J. Griffith, Krishna Feron, Nicolas C. Nicolaidis, Nathan A. Cooling, Xiaojing Zhou, John Holdsworth, Warwick J. Belcher, and Paul C. Dastoor. The origin of performance limitations in miniemulsion nanoparticulate organic photovoltaic devices. 175:77–88. ISSN 09270248. doi: 10.1016/j.solmat.2017.09.007. URL <https://linkinghub.elsevier.com/retrieve/pii/S0927024817304968>.
- [48] Kyra N. Schwarz, Sam B. Farley, Trevor A. Smith, and Kenneth P. Ghiggino. Charge generation and morphology in p3ht : PCBM nanoparticles prepared by mini-emulsion and reprecipitation methods. 7(47):19899–19904. ISSN 2040-3364, 2040-3372. doi: 10.1039/C5NR06244F. URL <http://xlink.rsc.org/?DOI=C5NR06244F>.
- [49] Natasha A.D. Yamamoto, Margaret E. Payne, Marlus Koehler, Antonio Facchetti, Lucimara S. Roman, and Ana C. Arias. Charge transport model for photovoltaic devices based on printed polymer: Fullerene nanoparticles. 141:171–177. ISSN 09270248. doi: 10.1016/j.solmat.2015.05.034. URL <https://linkinghub.elsevier.com/retrieve/pii/S0927024815002457>.
- [50] Valmore S. Rodriguez, Mohamed S. El-Aasser, Jose M. Asua, and Cesar A. Silebi. Miniemulsion copolymerization of styrene–methyl methacrylate. 27(11):3659–3671. ISSN 0887624X, 10990518. doi: 10.1002/pola.1989.080271109. URL <https://onlinelibrary.wiley.com/doi/10.1002/pola.1989.080271109>.
- [51] Christian Müller. On the glass transition of polymer semiconductors and its impact on polymer solar cell stability. 27(8):2740–2754. ISSN 0897-4756, 1520-5002. doi: 10.1021/acs.chemmater.5b00024. URL <https://pubs.acs.org/doi/10.1021/acs.chemmater.5b00024>.
- [52] Natalie P. Holmes, Melissa Marks, James M. Cave, Krishna Feron, Matthew G. Barr, Adam Fahy, Anirudh Sharma, Xun Pan, David A. L. Kilcoyne, Xiaojing Zhou, David A. Lewis, Mats R. Andersson, Jan van Stam, Alison B. Walker, Ellen Moons, Warwick J. Belcher, and Paul C. Dastoor. Engineering two-phase and three-phase microstructures from water-based dispersions of nanoparticles for eco-friendly polymer solar cell applications. 30(18):6521–6531, . ISSN 0897-4756, 1520-5002. doi: 10.1021/acs.chemmater.8b03222. URL <https://pubs.acs.org/doi/10.1021/acs.chemmater.8b03222>.
- [53] Andrew Stapleton, Ben Vaughan, Bofei Xue, Elisa Sesa, Kerry Burke, Xiaojing Zhou, Glenn Bryant, Oliver Werzer, Andrew Nelson, A.L. David Kilcoyne, Lars Thomsen, Erica Wanless, Warwick Belcher, and Paul Dastoor. A multilayered approach to polyfluorene water-based organic photovoltaics. 102:114–124. ISSN 09270248. doi: 10.1016/j.solmat.2012.03.016. URL <https://linkinghub.elsevier.com/retrieve/pii/S0927024812001225>.
- [54] Thomas Kietzke, Dieter Neher, Katharina Landfester, Rivelino Montenegro, Roland Güntner, and Ullrich Scherf. Novel approaches to polymer blends based on polymer nanoparticles. 2(6):408–412. ISSN 1476-1122, 1476-4660. doi: 10.1038/nmat889. URL <http://www.nature.com/articles/nmat889>.

- [55] Syahrul Ulum, Natalie Holmes, Matthew Barr, A.L.David Kilcoyne, Bill Bin Gong, Xiaojing Zhou, Warwick Belcher, and Paul Dastoor. The role of miscibility in polymer:fullerene nanoparticulate organic photovoltaic devices. 2(5):897–905, . ISSN 22112855. doi: 10.1016/j.nanoen.2013.03.009. URL <https://linkinghub.elsevier.com/retrieve/pii/S221128551300044X>.
- [56] Syahrul Ulum, Natalie Holmes, Darmawati Darwis, Kerry Burke, A.L. David Kilcoyne, Xiaojing Zhou, Warwick Belcher, and Paul Dastoor. Determining the structural motif of p3ht:PCBM nanoparticulate organic photovoltaic devices. 110:43–48, . ISSN 09270248. doi: 10.1016/j.solmat.2012.11.015. URL <https://linkinghub.elsevier.com/retrieve/pii/S0927024812005235>.
- [57] Hafiz Bilal Naveed, Ke Zhou, and Wei Ma. Interfacial and bulk nanostructures control loss of charges in organic solar cells. 52(10):2904–2915. ISSN 0001-4842, 1520-4898. doi: 10.1021/acs.accounts.9b00331. URL <https://pubs.acs.org/doi/10.1021/acs.accounts.9b00331>.
- [58] Gavvalapalli Nagarjuna, Mina Baghgar, Joelle A. Labastide, Dana D. Algaier, Michael D. Barnes, and Dhandapani Venkataraman. Tuning aggregation of poly(3-hexylthiophene) within nanoparticles. 6(12):10750–10758. ISSN 1936-0851, 1936-086X. doi: 10.1021/nn305207b. URL <https://pubs.acs.org/doi/10.1021/nn305207b>.
- [59] Bin Tan, Yancen Li, Maria Francisca Palacios, Joel Therrien, and Margaret J. Sobkowicz. Effect of surfactant conjugation on structure and properties of poly(3-hexylthiophene) colloids and field effect transistors. 488:7–14. ISSN 09277757. doi: 10.1016/j.colsurfa.2015.10.002. URL <https://linkinghub.elsevier.com/retrieve/pii/S0927775715302624>.
- [60] Jangwhan Cho, Seongwon Yoon, Kyu Min Sim, Yong Jin Jeong, Chan Eon Park, Soon-Ki Kwon, Yun-Hi Kim, and Dae Sung Chung. Universal selection rule for surfactants used in miniemulsion processes for eco-friendly and high performance polymer semiconductors. 10(11):2324–2333. ISSN 1754-5692, 1754-5706. doi: 10.1039/C7EE01943B. URL <http://xlink.rsc.org/?DOI=C7EE01943B>.
- [61] Natalie P. Holmes, Syahrul Ulum, Prakash Sista, Kerry B. Burke, Mitchell G. Wilson, Mihaela C. Stefan, Xiaojing Zhou, Paul C. Dastoor, and Warwick J. Belcher. The effect of polymer molecular weight on p3ht:PCBM nanoparticulate organic photovoltaic device performance. 128:369–377, . ISSN 09270248. doi: 10.1016/j.solmat.2014.05.046. URL <https://linkinghub.elsevier.com/retrieve/pii/S0927024814003043>.
- [62] Xu Han, Monojit Bag, Timothy S. Gehan, Dhandapani Venkataraman, and Dimitrios Maroudas. Analysis of hole transport in thin films and nanoparticle assemblies of poly(3-hexylthiophene). 610-611:273–277. ISSN 00092614. doi: 10.1016/j.cplett.2014.07.022. URL <https://linkinghub.elsevier.com/retrieve/pii/S0009261414006009>.
- [63] Darmawati Darwis, Elisa Sesa, Syahrul Ulum, Natalie P. Holmes, Krishna Feron, Mahir Thameel, Riku Chowdhury, Dedy Farhamsah, Levi Tegg, Xiaojing Zhou, Paul C. Dastoor, and Warwick J. Belcher. Role of morphology of surfactant-free

- nanoparticles in organic photovoltaics. 49(7):4168–4179. ISSN 0361-5235, 1543-186X. doi: 10.1007/s11664-020-08144-4. URL <http://link.springer.com/10.1007/s11664-020-08144-4>.
- [64] Jiamo Guo, Hideo Ohkita, Hiroaki Benten, and Shinzaburo Ito. Near-IR femtosecond transient absorption spectroscopy of ultrafast polaron and triplet exciton formation in polythiophene films with different regioregularities. 131(46):16869–16880,. ISSN 0002-7863, 1520-5126. doi: 10.1021/ja906621a. URL <https://pubs.acs.org/doi/10.1021/ja906621a>.
- [65] Hideo Ohkita and Shinzaburo Ito. Transient absorption spectroscopy of polymer-based thin-film solar cells. 52(20):4397–4417. ISSN 00323861. doi: 10.1016/j.polymer.2011.06.061. URL <https://linkinghub.elsevier.com/retrieve/pii/S0032386111006215>.
- [66] Yasunari Tamai, Yuu Matsuura, Hideo Ohkita, Hiroaki Benten, and Shinzaburo Ito. One-dimensional singlet exciton diffusion in poly(3-hexylthiophene) crystalline domains. 5(2):399–403. ISSN 1948-7185, 1948-7185. doi: 10.1021/jz402299a. URL <https://pubs.acs.org/doi/10.1021/jz402299a>.
- [67] Natalie P. Holmes. Questions about p3ht:PCBM studies.
- [68] Jiamo Guo, Hideo Ohkita, Seiichirou Yokoya, Hiroaki Benten, and Shinzaburo Ito. Bimodal polarons and hole transport in poly(3-hexylthiophene):fullerene blend films. 132(28):9631–9637,. ISSN 0002-7863, 1520-5126. doi: 10.1021/ja9108787. URL <https://pubs.acs.org/doi/10.1021/ja9108787>.
- [69] A. Hartschuh, H. Port, and H.C. Wolf. Polarized fs transient absorption of CT states in an-PMDA crystals—excitonic strings? 94-95:441–445. ISSN 00222313. doi: 10.1016/S0022-2313(01)00333-7. URL <https://linkinghub.elsevier.com/retrieve/pii/S0022231301003337>.
- [70] Omar M. Awartani, Bhoj Gautam, Wenchao Zhao, Robert Younts, Jianhui Hou, Keenan Gundogdu, and Harald Ade. Polymer non-fullerene solar cells of vastly different efficiencies for minor side-chain modification: impact of charge transfer, carrier lifetime, morphology and mobility. 6(26):12484–12492. ISSN 2050-7488, 2050-7496. doi: 10.1039/C7TA01746D. URL <http://xlink.rsc.org/?DOI=C7TA01746D>.

Appendices

Appendix A

Artifact

Consistent dips in ΔA around 950nm are observed in all NIR data. These dips are not features observed in literature. The raw data in Figure A.1 shows the light spectrum generated by the probe laser after passing through the crystal.

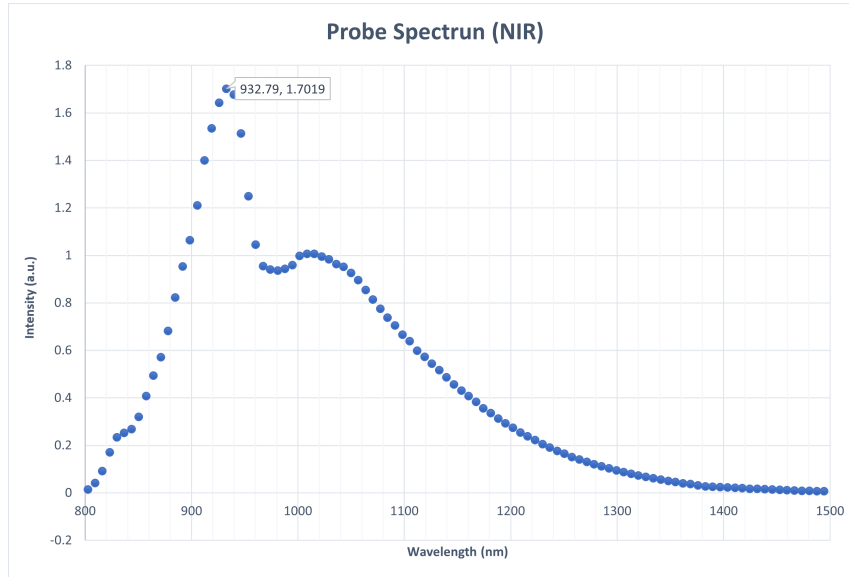


Figure A.1: Snapshot of the NIR light spectrum generated by the probe laser.
The wavelength of the peak value is shown.

This spectrum observes a sharp peak around 933nm, giving reason to believe the spectrometer saturates in that region when the probe pulse is applied with no pump. The result is a lower ΔA value when compared to the pump/probe pulses. Artefacts in TA due to saturation are a known effect.

Appendix B

PBDB-T:ITIC Cell Data

Since the nanoparticle inks were having issues in addition to ongoing lab closures due to coronavirus, Dr. Clark and I decided to pursue an alternate project. This involved working with two researchers - Emma Spooner and Rachel Kilbride - on an existing project. The project, which addresses a similar issue, involved differences in cells using ‘greener’ solvents like ortho-xylene and carbon disulfide plus acetone (CSA). The organic solar cell would use the donor PBDB-T and non-fullerene acceptor ITIC blended using different solvents.

My contribution was to analyze the photophysics of these active layers using TA. The films produced by Emma were encapsulated by me in a glovebox in Hicks C6. These films, as well as solutions of PBDB-T and ITIC in ortho-xylene, were TA samples for the HELIOS laser setup. In addition, Solstice laser setup was used for TA over a longer timescale (-5ns – 10 μ s. In both experiments, the pump excitation wavelength was 532 nm. The results are presented below.

B.1 Steady-State Spectroscopy

Figure B.1 shows normalized steady-state spectroscopy. There were 12 encapsulated films in total representing 4 different solvents and 3 different material combinations (neat PBDB-T, neat ITIC, and a PBDB-T:ITIC blend). When added as a 1:1 combination, the individual components appear to come close to the absorption for a blend in chlorobenzene and chloroform. In ortho-Xylene and CS₂ + Acetone, there is a more prominent peak around 1.75 eV. This is likely due to a greater proportion of ITIC, which may have arisen out of solubility issues between the solvent and the PBDB-T.

Turning to the material combinations under different solvents (Figure B.2), the spectra are largely similar. Being clear, the solvents were unlikely to have a profound effect on the absorption spectra in the UV-Visible region. The amount of absorption in the o-Xylene blend around 1.75eV is again more prominent. The overlap in the peak energies suggests strong fundamental similarities in the composition of the films. Peak values are also consistent with literature.[17]

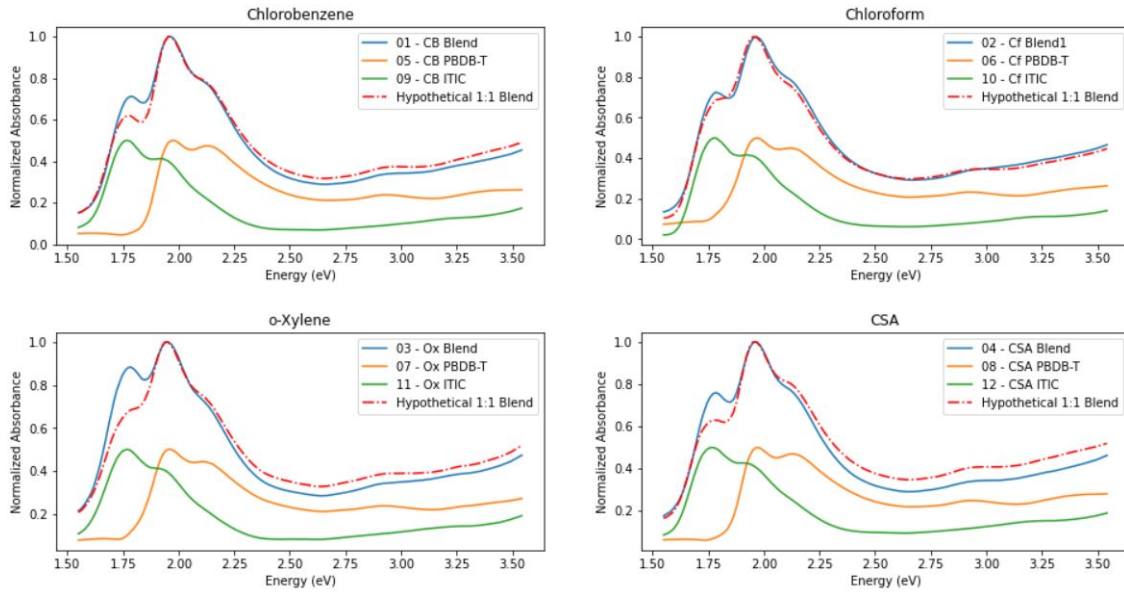


Figure B.1: Normalized spectra from films produced for each solvent (listed in the graph title). The films that contained neat PBDB-T and neat ITIC were normalized to 0.5 then added to produce the hypothetical 1:1 blend.

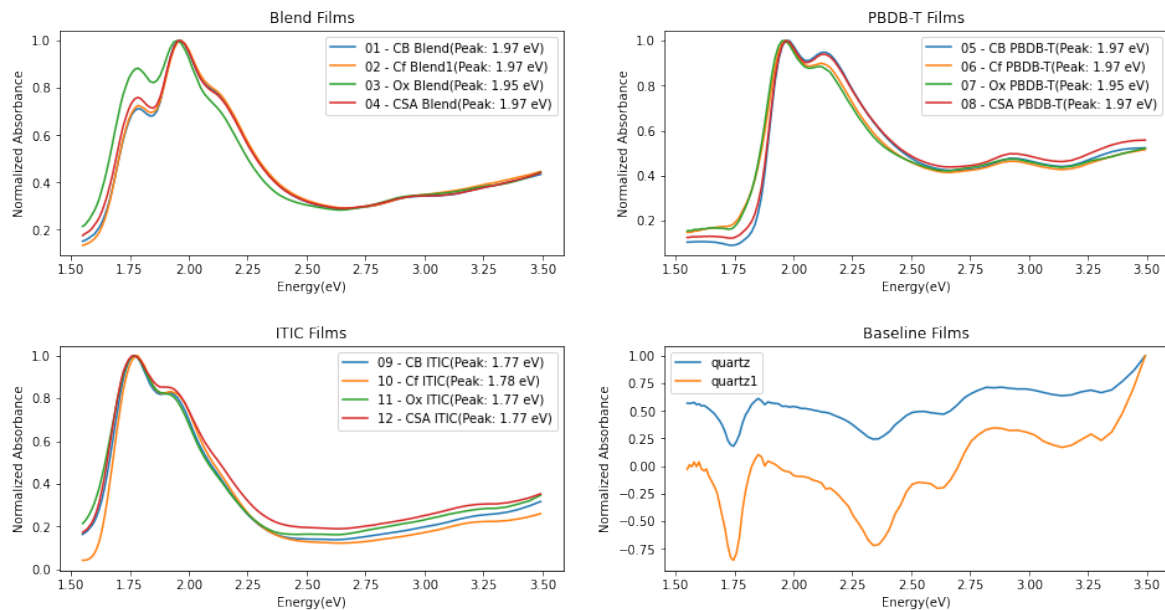


Figure B.2: Normalized spectra from films produced from different material combinations (listed in title). The baseline films graph has no particular meaning.

B.2 TA Spectroscopy

Awatarni et al (2018) assign several features to PBDB-T:ITIC films using TA spectroscopy.[70] The PBDB-T exciton is assigned to 1.08eV, the ITIC exciton is assigned to 1.28eV. The polaron is assigned 1.32eV.

In the neat PBDB-T and neat ITIC films shown in Figure B.3, the exciton features are prominent and in good agreement. The PBDB-T exciton is seen at 1.07eV, the ITIC exciton is seen at 1.27eV. Both have fairly quick decay times – the ITIC exciton is almost completely gone by 500ps. There is an absence of any feature at 1.32eV, excepting residual signal from the excitons.

This 1.32eV feature is observed in the blend films in Figure B.4. (The abbreviations used in the blend films are CB – Chlorobenzene; CF – Chloroform; OX – ortho-Xylene; and CSA – Carbon Disulfide and Acetone.) Looking at the blend TA spectra, after a few nanosecond, the exciton features have mainly subsided. The remaining signal at 1.32 eV can be seen in all blend films, supporting its assignment as a charge feature (free polaron).

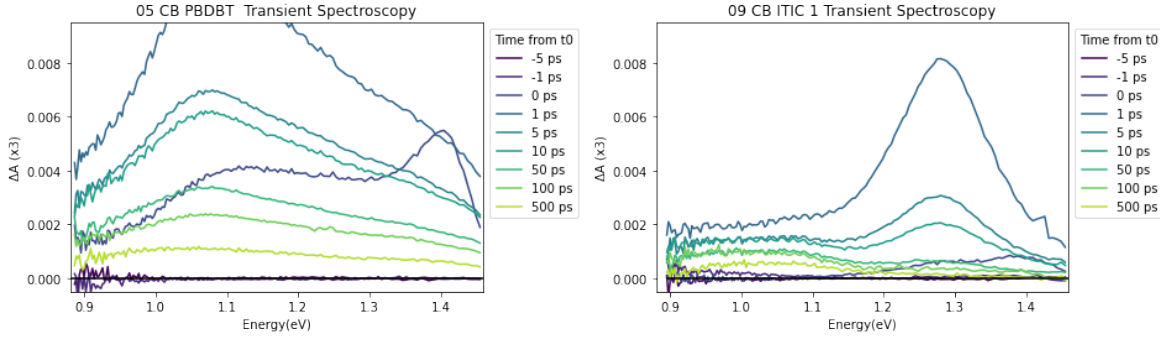


Figure B.3: Transient absorption graphs of films using chlorobenzene solvent – (a) neat PBDB-T and (b) neat ITIC. Note the peak feature of the PBDB-T exciton at 1.08eV, and the peak feature of the ITIC exciton at 1.28eV.

B.2.1 Long-Time TA

Due to the nature of the Solstice, long-time TA data was only able to be captured in the UV-Vis spectrum. The long-time TA device measures $\frac{\Delta T}{T}$ rather than ΔA . This is comparable, though not equivalent, to flipping the graph over the x-axis. In the first figure, there is a large absorption feature (likely due to charge states) peaking around 2.45eV. Between the $100\mu\text{W}$ and $500\mu\text{W}$ pump fluences, a new positive charge feature is observed around 2.28eV, while 2.32eV remains relatively steady around 0. Although Figure B.5 only displays the long-time TA features for the chlorobenzene blend, this sudden 2.28eV feature at $500\mu\text{W}$ pump power is also present in chloroform and $\text{CS}_2 + \text{Acetone}$ blends.

Kinetics

Viewed kinetically, the charge feature observed in several solvent blends at 2.45eV is a point of interest. Kinetic graphs here will follow a symlog-log scaling. Generally speaking, decay patterns tend to follow a constant increase or decrease in signal strength with higher pump

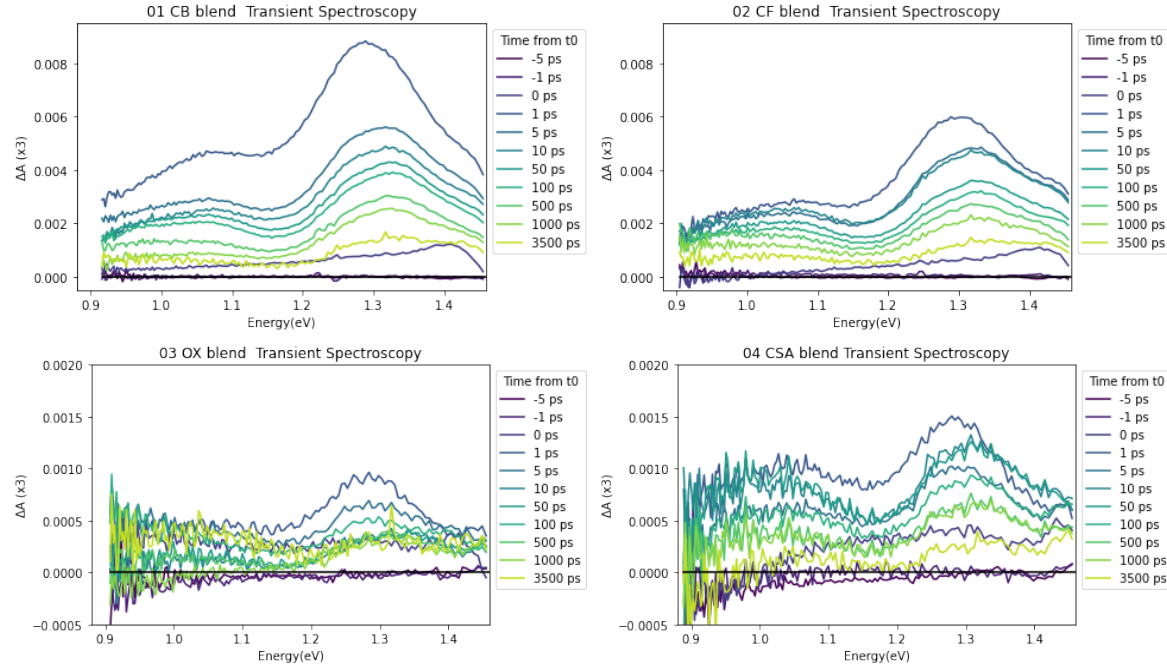


Figure B.4: Transient absorption graphs for blend films using different solvents (listed in the graph titles).

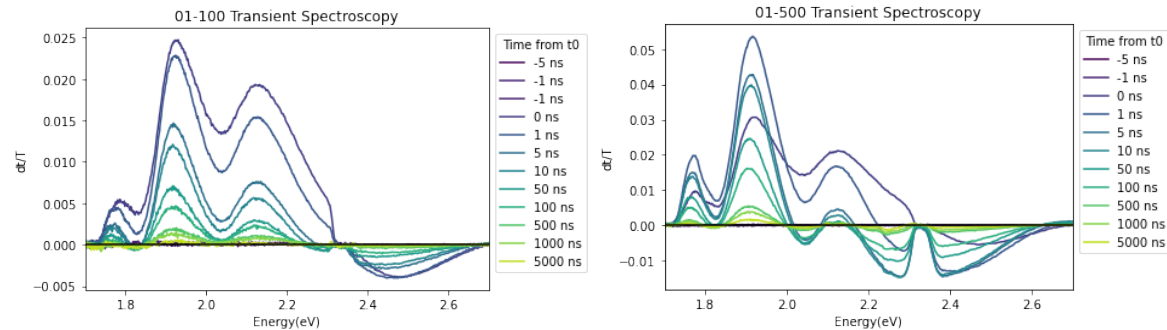


Figure B.5: Long-time TA spectra for chlorobenzene films taken at a pump power of (a) $100\mu\text{W}$ and (b) $500\mu\text{W}$.

power. If geminate recombination is dominant, then no change would be observed, as with chlorobenzene. For three of our four solvent blends shown in Figure B.6, the $500\mu\text{W}$ pump power feature appears to stand out from the other curves. ortho-Xylene is the only solvent blend that continues with the usual monotonic trend.

Another point of note (seen in Figure B.7) is that while this 2.45eV charge feature decays similarly in all blend films at $100\mu\text{W}$ pump power, at $10\mu\text{W}$, the solvent blend decay patterns begin to separate.

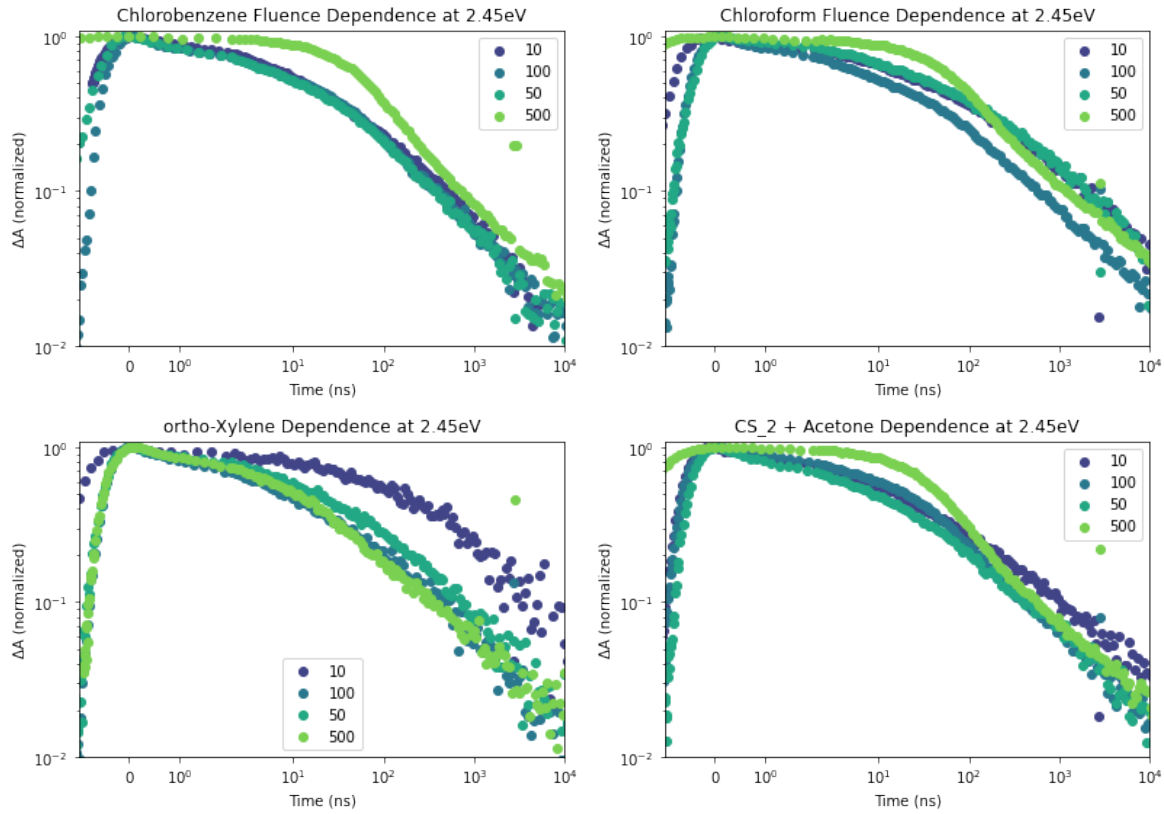


Figure B.6: Kinetic graphs for different solvent blends (listed in graph titles) at 2.45eV. The values in the legend (and colors) refer to the pump power in μW for the dataset.

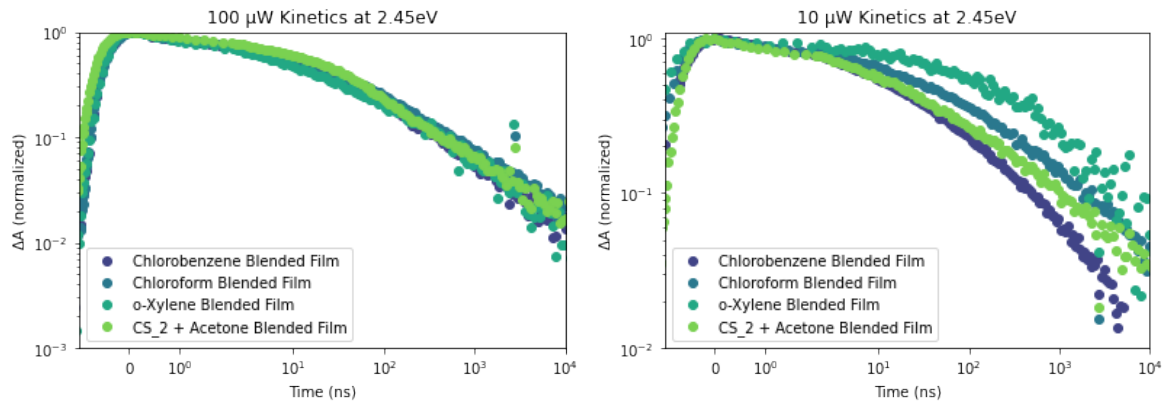


Figure B.7: Kinetics graphs comparing the 2.45eV feature for all different solvents at the same pump power – (a) 100 μW and (b) 10 μW .